The Astronomical Journal, 166:168 (21pp), 2023 October https://doi.org/10.3847/1538-3881/acef1e
© 2023. The Author(s). Published by the American Astronomical Society.
OPEN ACCESS

Modified Newtonian Dynamics as an Alternative to the Planet Nine Hypothesis

Katherine Brown[1] and Harsh Mathur[2]
[1] Physics Department, Hamilton College, 198 College Hill Road, Clinton, NY 13323, USA
[2] Physics Department, Case Western Reserve University, 10900 Euclid Avenue, Cleveland, OH 44106, USA
Received 2022 August 4; revised 2023 July 26; accepted 2023 August 9; published 2023 September 22

Abstract

A new class of Kuiper Belt objects (KBOs) that lie beyond Neptune with semimajor axes greater than 250 astronomical units show orbital anomalies that have been interpreted as evidence for an undiscovered ninth planet. We show that a modified gravity theory known as modified Newtonian dynamics (MOND) provides an alternative explanation for the anomalies using the well-established secular approximation. We predict that the major axes of the orbits will be aligned with the direction toward the Galactic center and that the orbits cluster in phase space, in agreement with observations of KBOs from the new class. Thus, MOND, which can explain galactic rotation without invoking dark matter, might also be observable in the outer solar system.

Unified Astronomy Thesaurus concepts: Modified Newtonian dynamics (1069); Kuiper belt (893)

1. Introduction

An exciting development in outer solar system studies is the discovery of a new class of Kuiper Belt objects (KBOs) with orbits that lie outside that of Neptune and have semimajor axes in excess of 250 au (Brown et al. 2004; Trujillo & Sheppard 2014; Batygin et al. 2019). The alignment of the major axes of these objects and other orbital anomalies are the basis for the hypothesis that a planet about 5–10 times as massive as Earth orbits the Sun at an average distance of 500 au (Batygin & Brown 2016a, 2016b; Malhotra et al. 2016; Batygin et al. 2019; Brown & Batygin 2016, 2019). Here we argue that a modified gravity theory known as modified Newtonian dynamics (MOND; Milgrom 1983; Famaey & McGaugh 2012; Banik & Zhao 2022) provides an alternative explanation for the observed alignment, owing to significant quadrupolar and octupolar terms in the MOND galactic field within the solar system (Milgrom 2009) that are absent in Newtonian gravity. We show using the well-established secular approximation (Murray & Dermott 2000) that MOND predicts a population of KBOs with orbits whose major axes are aligned along the direction toward the center of the galaxy and with aphelia oriented toward the galactic center. Moreover, this population is predicted to cluster in phase space: the orbits should have high eccentricity and a propensity for their minor axes to be perpendicular to the direction to the center of the galaxy. All of these features are exhibited by known KBOs belonging to the newly discovered class, in support of the MOND hypothesis. MOND was originally developed to explain galaxy rotation, and its predictions on the galactic scale have recently been subject to stringent observational tests (McGaugh et al. 2016; Chae et al. 2020). Progress has also been made in applying MOND on the cosmological scale (Skordis & Zlosnik 2021). Hence evidence of MOND on solar system scales would further strengthen the case for it, and establish the Kuiper Belt as a laboratory for studying important questions of fundamental physics.

Original content from this work may be used under the terms of the Creative Commons Attribution 4.0 licence. Any further distribution of this work must maintain attribution to the author(s) and the title of the work, journal citation and DOI.

In the quasilinear formulation of MOND (Milgrom 2010), the Newtonian gravitational field $\boldsymbol{g}_N$ is modified with an interpolating function ν to produce a "pristine" field $\boldsymbol{g}_P = \nu(g_N/a_0)\boldsymbol{g}_N$ where a_0 is a fundamental acceleration scale. The interpolating function may induce a curl on the pristine field; $\boldsymbol{g}_Q$ is the curl-free part of $\boldsymbol{g}_P$, and it is the physical field: in the absence of other forces, a test mass would experience acceleration $\boldsymbol{g}_Q$. The interpolating function obeys $\nu(x) \to 1$ as $x \to \infty$ so that Newtonian gravity is recovered when the gravitational field is strong compared to a_0 and $\nu(x) \to x^{-1/2}$ as $x \to 0$ in the weak field regime to ensure consistency with galaxy rotation curves. We take $\nu = 1/[1 - \exp(-\sqrt{x})]$, the same form that is used by Lelli et al. (2017); see also Zhu et al. (2023). This form has the right asymptotic behavior and is consistent with astrophysical and solar system constraints. For a point mass M the characteristic MOND radius is given by $R_M = (GM/a_0)^{1/2}$; this is the distance at which the field crosses over from the strong field Newtonian behavior to an MOND regime. Using $a_0 = 1.2 \times 10^{-10}$ m s^{-2} (the best fit to galaxy rotation data; McGaugh et al. 2016) and the mass of the Sun $M = M_\odot$, we find the MOND radius for the Sun $R_M = 7000$ au. This provides the first clue that MOND effects may be detectable in the Kuiper Belt.

2. Galactic Field and the Phantom Mass

In Newtonian gravity, the galactic field is essentially uniform on solar system scales and does not affect the observable relative motion of solar system bodies since they all accelerate equally in response to it. Tidal effects from nonuniformities in the galactic field are relevant to the Oort cloud but not the Kuiper Belt (Heisler & Tremaine 1986). The combined field of the Sun at distance r and the galaxy is thus

$$\boldsymbol{g}_N = -\hat{\boldsymbol{r}}\frac{GM_\odot}{r^2} + \boldsymbol{\gamma}_N \tag{1}$$

where $\boldsymbol{\gamma}_N$ is the galactic field. In MOND however, there is an additional anomalous field $\boldsymbol{g}_A$ within the solar system that can be interpreted as being due to a "phantom" mass density $\rho_{\rm ph}$

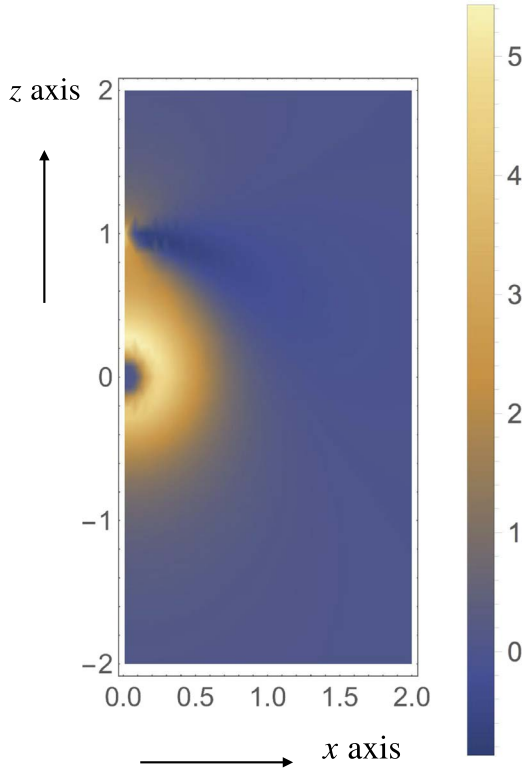

Figure 1. *Phantom mass distribution.* The phantom mass is rotationally symmetric about the z-axis and is localized at distances comparable to the MOND radius R_M. The Sun is at the origin, and the galactic center is on the positive z-axis. Distance along the axes is marked in units of $R_M = 7000$ au, and the density $\rho_{\rm ph}$ is in units of $M_\odot/(4\pi R_M^3)$. We take $\gamma_N = 0.9\, a_0$ consistent with the acceleration of the Sun toward the center of the galaxy (McGaugh 2018). An interesting feature is that the phantom mass distribution changes sign near the point where the Newtonian field of the galaxy and the Sun add up to zero.

(Milgrom 2009)

$$\rho_{\rm ph} = -\frac{1}{4\pi G}\boldsymbol{g}_N \cdot \nabla\nu(g_N/a_0); \tag{2}$$

see Appendix B. The relative motion of objects in the solar system is influenced by the anomalous MOND field $\boldsymbol{g}_A$, a phenomenon called the external field effect (Bekenstein & Milgrom 1984) that has been recently observed on the galactic scale (Chae et al. 2020, 2021; Petersen & Lelli 2020; Asencio et al. 2022; Chae 2022). Unlike dark matter, the phantom mass has no independent dynamics; it is completely determined by the visible matter that produces $\boldsymbol{g}_N$. Figure 1 shows the phantom mass distribution corresponding to the Newtonian field in Equation (1). Asymptotically, $\rho_{\rm ph}$ falls off as a power law for $r \gg R_M$ and exponentially for $r \ll R_M$; there is essentially no phantom mass in the inner solar system.

We can compute the potential ψ_A defined via $\boldsymbol{g}_A = -\nabla\psi_A$ using a multipole expansion (S.I. Section C). To leading order, the potential of a mass distribution localized far from the origin is given by the quadrupole term

$$\psi = -\frac{fGM}{R^3} r^2 P_2(\cos\theta) \tag{3}$$

where f is a geometric factor, M and R the mass and length scales, respectively, that characterize the distribution, and P_2 is the second-order Legendre polynomial. We have assumed the mass distribution is rotationally symmetric about the z-axis and $r \ll R$. For the phantom mass distribution $M = M_\odot$, $R = R_M$ and $f = q_2/4\pi$ where q_2 is a constant of order unity that depends on γ_N/a_0 and the form of ν. For our choice of ν and $\gamma_N/a_0 = 1.20$, we find $q_2 = 1.00$ by numerical integration. This value of q_2 is of the same order of magnitude as the Cassini bound (Hees et al. 2014), though it is numerically larger than the bound. Other interpolating functions are shown by Hees et al. (2016) to be consistent with the Cassini bound. Since here we are only interested in an order-of-magnitude comparison, we may take q_2 to be of order unity.

To compare the effect of this quadrupole field on a KBO with that of the hypothetical Planet Nine, we use the secular approximation (Murray & Dermott 2000), wherein the mass of a planet is distributed nonuniformly along its orbit. The amount of mass on an arc of orbit is proportional to the time required for the planet to traverse the arc. The quadrupolar field of Planet Nine in this approximation is also given by Equation (3) with $M = m_9$ and $R = a_9$ (the mass and semimajor axis, respectively, of Planet Nine) and $f = -(1 - e_9^2)^{-3/2}$ where e_9 is the eccentricity of the Planet Nine orbit (S.I. Section C). Note that the quadrupoles for MOND and Planet Nine are of opposite sign. Taking representative values for the parameters from Batygin et al. (2019; $m_9 = 5$ Earth masses, $a_9 = 500$ au, and $e_9 = 0.25$), we find that the orbit-averaged quadrupole moment for Planet Nine and MOND are the same order of magnitude. This provides further indication that MOND could have a significant effect on the orbits of KBOs.

3. MOND and the Outer Kuiper Belt

We now analyze the effects of the MOND field on the orbit of a KBO of mass m_K using the secular approximation. Under the influence of the Sun alone, a KBO would move along a Keplerian ellipse, with six orbital elements: semimajor axis a_K, eccentricity e_K, three Euler angles (ω_K, i_K, Ω_K), and the "mean anomaly," which specifies where on the ellipse the KBO is located. We work in a frame with the Sun at the origin and the center of the galaxy located along the positive z-axis. In its reference configuration, the KBO orbit is assumed to lie in the x–y plane with the perihelion on the positive x-axis. The orientation (ω_K, i_K, Ω_K) corresponds to the orbit being rotated from the reference orientation successively about the z-axis by ω_K, the x-axis by i_K and about the z-axis again by Ω_K. In the secular approximation, the dynamics has two important simplifications (Murray & Dermott 2000): a_K is conserved, and the mean anomaly has no effect on the dynamics of the other orbital elements. The four remaining dynamical variables, e_K and the Euler angles, undergo slow evolution due to the MOND perturbation.

In the secular approximation, the dynamics of the orbit is controlled by a "disturbing function," which is the gravitational potential energy of the orbit-distributed mass of the KBO and the phantom mass distribution. This potential energy may be written in the form of a multipole expansion (Appendix D). The disturbing function is often calculated in an approximate expansion in eccentricity or inclination (Murray & Dermott 2000), but we need the quadrupole and octupole terms exactly. We have developed an efficient method to obtain these exact expressions. To quadrupole order, the secular disturbing

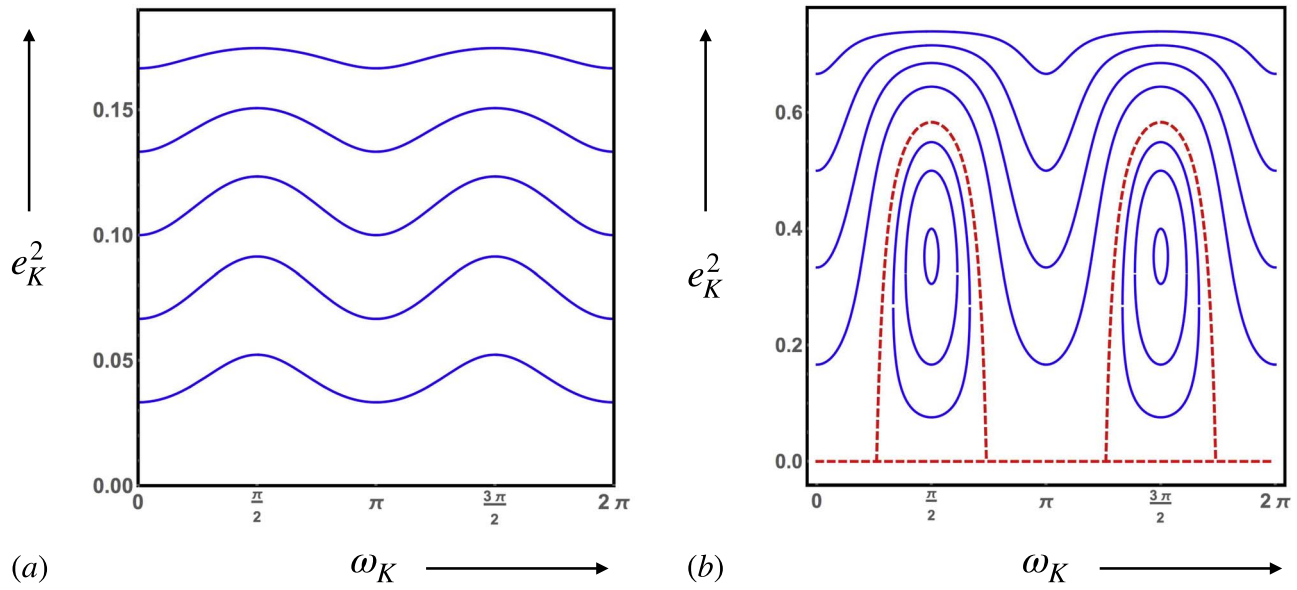

Figure 2. Orbital dynamics in the quadrupole approximation. (a) Contours of fixed $\mathcal{S}_Q^{\rm eff}$ are wavy lines that extend across the (e_K^2, ω_K) plane for $3/5 \leqslant h^2 \leqslant 1$. (b) For $0 \leqslant h^2 < 3/5$, the phase space is dominated by two fixed points. The contours of fixed $S_Q^{\rm eff}$ are loops around the fixed points but remain wavy lines on the other side of the separatrix shown in red. The orbital elements thus precess along the wavy lines or oscillate about the fixed-point values around the loops. The phase-space flow is along the contours clockwise around the loops and from left to right (increasing ω_K) along the wavy lines. The timescale of the dynamics is 10^7 yr for a KBO orbit with a semimajor axis of 1000 au.

function is

$$\mathcal{R}_Q = \frac{Gm_K M_\odot}{R_M}\left(\frac{a_K}{R_M}\right)^2 \frac{q_2}{32\pi}\mathcal{S}_Q \tag{4}$$

where

$$\begin{aligned}\mathcal{S}_Q = &-2 - 3e_K^2 + 15e_K^2\cos(2\omega_K) + 6\cos^2 i_K \\ &+ 9e_K^2\cos^2 i_K - 15e_K^2\cos(2\omega_K)\cos^2 i_K.\end{aligned} \tag{5}$$

The octupole term and the derivation of the quadrupole and octupole terms are given in Appendix D.

Due to the cylindrical symmetry of the anomalous field, the secular disturbing function is independent of Ω_K. As a result, the component of the orbital angular momentum along the symmetry axis, $(GM_\odot m_K a_K)^{1/2}h$ is conserved. Here the scaled angular momentum

$$h = \sqrt{1 - e_K^2}\cos i_K. \tag{6}$$

Hence we have two conserved quantities, h and $\mathcal{S}_Q$ itself, so the MOND dynamics of KBO orbits is integrable. We can eliminate $\cos i_K$ from $\mathcal{S}_Q$ using Equation (6) to obtain an expression for $\mathcal{S}_Q^{\rm eff}$ that depends only on e_K and ω_K.

The orbital evolution can be visualized by plotting contours of fixed $\mathcal{S}_Q^{\rm eff}$ in the (e_K, ω_K) phase plane. Figure 2 shows that for $0 \leqslant h^2 \leqslant 3/5$, the phase space is dominated by two fixed points located at $(e_C, \pi/2)$ and $(e_C, 3\pi/2)$ where $e_C^2 = 1 - \sqrt{5/3}\,|h|$. Over this range of h, the contours encircle the fixed points, which are separated from a region of phase space where the contours are wavy lines extending across the phase plane. By use of Lagrange's equations we can show that the phase-space flow is from left to right along the wavy lines (i.e., ω_K increases monotonically in time) while the loops are traversed clockwise (Appendix E). The effect of the octupole term is to break the symmetry between the fixed points: the one at $(e_C, \pi/2)$ becomes less stable while the one at $(e_C, 3\pi/2)$ becomes more stable. The dynamics of i_K is dictated by Equation (E3), and Ω_K undergoes precession (monotonic increase in time) regardless of the value of $|h|$ (Appendix E).

Next we consider the effect of integrability-breaking terms on the orbital dynamics. These terms include nonsecular terms in the MOND disturbing function and the secular and nonsecular perturbations produced by the giant planets. Because of the long timescales involved, it is also important to take into account the slow variation of the direction toward the center of the galaxy. According to Hamiltonian chaos theory (Percival & Richards 1983) the phase-space flow will become chaotic under the perturbations, but a regular flow should persist around the stable fixed point near $(e_C, 3\pi/2)$, particularly for small values of h. (For a given a_K, there is a minimum value of $|h|$ needed to ensure that the orbit does not penetrate the inner solar system; see Appendix E.)

Thus we arrive at our central result: we predict the existence of a population of KBOs that are localized near the fixed point $(e_C, 3\pi/2)$. For small h, these orbits have inclinations $i_K \approx \pi/2$. For an orbit with $\omega_K = 3\pi/2$, the apsidal vector $\hat{\boldsymbol{\alpha}}_K$ (the unit vector that points from the Sun to the perihelion), then makes a small angle $\pi/2 - i_K$ with $-\hat{\boldsymbol{n}}_G$, where $\hat{\boldsymbol{n}}_G$ is the unit vector that points from the Sun to the center of the galaxy. Thus, we see that the apsidal vectors are aligned along the direction $-\hat{\boldsymbol{n}}_G$. Finally, note that due to precession in Ω_K, the orbits could have very high inclinations relative to the ecliptic.

4. Comparison to Data

We now examine to what extent KBOs of the newly discovered class (which we refer to as the Sedna family) conform to these predictions. Batygin et al. (2019) identified six members of the Sedna family that have stable orbits under the influence of the known planets, and eight more that are metastable. The stable KBOs are a particularly good testing ground for the Planet Nine hypothesis as well as the MOND hypothesis advanced here.

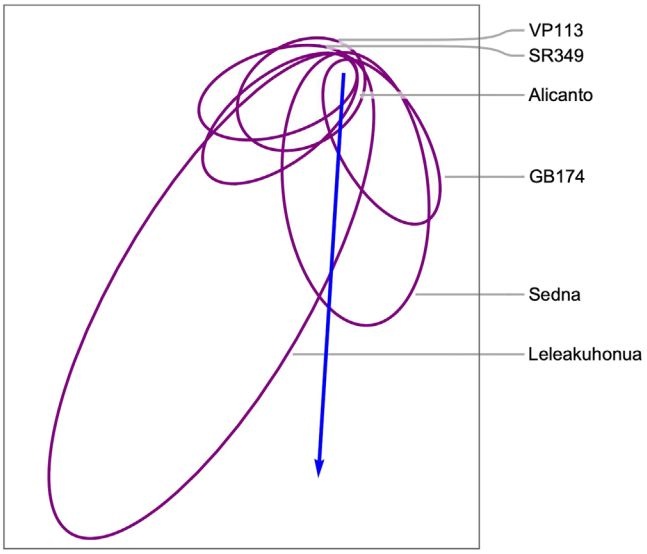

Figure 3. Orbital alignment. Orbits of six KBOs of the Sedna family projected onto the ecliptic plane. The blue line is drawn parallel to the projection of $\hat{\boldsymbol{n}}_G$ onto the ecliptic plane. The orbits and $\hat{\boldsymbol{n}}_G$ lie essentially in the ecliptic plane, so the projection does not induce significant distortion. The major axes of the orbits are seen to align with the direction to the center of the galaxy, with the aphelion oriented toward the Galactic center. This result is intuitively plausible since the aphelion is the heavy end of the orbit in secular perturbation theory. The KBO orbital parameters used to generate this plot are taken from the Minor Planet Database of the International Astronomical Union.

Figure 3 shows the six Sedna family orbits that are stable, projected onto the ecliptic plane. The well-documented alignment of the orbits (Brown & Batygin 2019) is evident, but the figure shows that the orbits are also aligned with the direction to the center of the galaxy. This observation has not been noted before and is a prediction of the MOND hypothesis. To quantify the alignment, we calculate $\hat{\boldsymbol{\alpha}}_K \cdot \hat{\boldsymbol{n}}_G$ for the six stable KBOs, and find a mean value of -0.68. The expected value of this quantity is zero in the absence of MOND, as there is otherwise no physical basis for a correlation between the apsidal vectors and the direction to the center of the galaxy. If we make the null hypothesis that the apsidal vectors of the KBOs are independent random variables uniformly distributed over the unit sphere, then the observed value of -0.68 is 3σ away from the expected value of zero. Alternatively, we note that according to the null hypothesis, the quantity $u = (1 + \hat{\boldsymbol{\alpha}}_K \cdot \hat{\boldsymbol{n}}_G)/2$ is a random variable uniformly distributed over the unit interval $0 \leqslant u \leqslant 1$. The six observed values of u deviate strongly from a uniform distribution. The Kolmogorov–Smirnov test shows that the observed deviation from a uniform distribution has a cumulative probability of only 0.0045; hence, the null hypothesis is falsified at a high level of confidence (see Appendix F). Our model does not require perfect antialignment between $\hat{\boldsymbol{\alpha}}_K$ and $\hat{\boldsymbol{n}}_G$; a crude estimate suggests that A_K, the angle between $\hat{\boldsymbol{\alpha}}_K$ and $\hat{\boldsymbol{n}}_G$, should lie in the range $130°$–$180°$ compatible with the data (Appendix F).

Sometimes, the longitude of perihelion $\varpi = \omega + \Omega$ is used as a proxy for apsidal alignment. However, ϖ correlates with alignment only for small inclinations, and it is a frame-dependent quantity. We prefer to quantify the alignment by calculating $\hat{\boldsymbol{\alpha}}_K \cdot \hat{\boldsymbol{n}}_G$ because it is an invariant quantity and is unambiguously a measure of alignment.

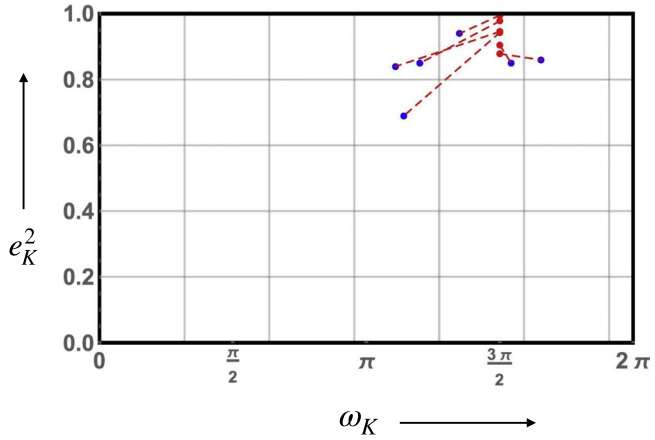

Figure 4. Phase-space clustering. Plot of (e_K^2, ω_K) for the six KBOs of the Sedna family (blue points) and the location of the corresponding fixed point of the MOND orbital dynamics in the quadrupole approximation (red points). The two points for each KBO have been connected by a dashed line to guide the eye. The KBO orbital parameters used to generate this plot are taken from the Minor Planet Database of the International Astronomical Union.

Figure 4 shows the orbital elements (e_K^2, ω_K) as well as the location of the fixed point $(e_C^2, 3\pi/2)$ for the six stable KBOs (see Appendix F for details). As expected, there is a clustering of the fixed points and KBO orbital elements.

Thus far we have concentrated on the six KBOs of the Sedna family that are known to have stable orbits under the influence of the known planets and that are therefore the best exemplars of the class. The review of Batygin et al. (2019) identifies eight more KBOs that have metastable orbits and since the publication of the review, eight additional KBOs that belong to the class have appeared in the Minor Planet Database. In Appendix F, we show that the alignment and phase-space clustering shown in Figures 3 and 4 persist when all 22 KBOs are included in the plots.

5. Conclusion

A larger sample of stable KBOs in the Sedna family compared to dynamical simulations would allow for further tests of the MOND hypothesis. The prospects for discovery of more Sedna-like objects are good. Existing surveys such as Dark Energy Survey (Sheppard & Trujillo 2016; Bernardinelli et al. 2020a), Transiting Exoplanet Survey Satellite (Rice & Laughlin 2020), and Outer Solar System Origins Survey (Bannister et al. 2016, 2018) as well as the forthcoming Vera Rubin Telescope (Schwamb et al. 2018a, 2018b) and CMB-S4 (Abazajian et al. 2016; Cowan et al. 2016) all have the requisite sensitivity. In addition to KBOs fast spacecraft are another promising probe of MOND in the outer solar system (Banik & Kroupa 2019; Penner 2020).

Historically, claimed gravitational anomalies in the solar system have almost invariably proven to be spurious under closer examination, albeit sometimes involving more than a century of debate and meticulous observation (Standish 1993; Turyshev et al. 2012; Batygin et al. 2019). But they have also led to the discovery of Neptune and helped establish general relativity. It is possible that the Kuiper Belt anomalies are evidence of Planet Nine, or that they are spurious (Lawler et al. 2017b; Shankman et al. 2017; Bernardinelli et al. 2020b; Napier et al. 2021); alternatively, they may be evidence for a modification of Newtonian gravity.

Acknowledgments

We thank Stacy McGaugh for helpful discussions and the two anonymous reviewers for suggesting references, helping improve the clarity of presentation, and recommending the use of the Kolmogorov–Smirnov test.

Appendix A
Review of MOND Field Equations

The gravitational field is described by a vector $\boldsymbol{g}$ that corresponds to the acceleration that would be experienced by a test mass due to gravity if no other forces were present. Newton's law of gravitation may then be written as the pair of field equations

$$\nabla \cdot \boldsymbol{g}_N = -4\pi G\rho \quad \text{and} \quad \nabla \times \boldsymbol{g}_N = 0. \tag{A1}$$

Here $\boldsymbol{g}_N$ is the Newtonian gravitational field produced by the mass density ρ, and G is Newton's gravitational constant.

In the quasilinear formulation of MOND (Milgrom 2010), given a mass distribution ρ, the first step is to calculate the Newtonian field $\boldsymbol{g}_N$ corresponding to that mass distribution. Next, one calculates the pristine field, which is related to the Newtonian field via the nonlinear relation

$$\boldsymbol{g}_P = \boldsymbol{g}_N \nu\left(\frac{g_N}{a_0}\right). \tag{A2}$$

Here $a_0 = 1.2 \times 10^{-12}\ \mathrm{m\,s^{-2}}$ is the MOND acceleration scale. The value we have taken for this parameter is the recent best fit to galaxy rotation data (McGaugh et al. 2016), but the value has in fact remained remarkably stable for decades (Begeman et al. 1991; Gentile et al. 2011).

The interpolating function ν has the asymptotic behavior

$$\nu(x) \to 1 \text{ for } x \gg 1 \quad \text{and} \quad \nu(x) \to \frac{1}{\sqrt{x}} \text{ for } x \ll 1. \tag{A3}$$

The $x \gg 1$ behavior is fixed by the requirement that at strong fields MOND should reduce to Newtonian gravity, and the $x \ll 1$ behavior by the requirement that the field of a point mass should fall off as $1/r$ at large distances. For specific computations in this paper, we have worked with the interpolating function

$$\nu(x) = \frac{1}{1 - \exp(-\sqrt{x})}. \tag{A4}$$

This form is consistent with galaxy rotation data and also with solar system constraints arising from the ephemerides of the known planets.

The next step is to compute the quasilinear field $\boldsymbol{g}_Q$, which is the curl-free part of $\boldsymbol{g}_P$. In MOND, the quasilinear field $\boldsymbol{g}_Q$ is the physical field: it is the acceleration experienced by test masses that are placed in the gravitational field. It is now helpful to define the mass density ρ_{eff}

$$-4\pi G\rho_{\mathrm{eff}} = \nabla \cdot \boldsymbol{g}_P. \tag{A5}$$

It then follows that $\boldsymbol{g}_Q$ obeys the field equations

$$\nabla \cdot \boldsymbol{g}_Q = -4\pi G\rho_{\mathrm{eff}} \quad \text{and} \quad \nabla \times \boldsymbol{g}_Q = 0. \tag{A6}$$

In other words, $\boldsymbol{g}_Q$ is the Newtonian field produced by the mass distribution ρ_{eff}. We may regard ρ_{eff} as the equivalent distribution of dark and visible matter that would be needed to mimic the effects predicted by MOND. However, MOND effects cannot always be mimicked by a suitable distribution of dark matter since ρ_{eff} is not necessarily positive.

As a simple illustration, consider the field of a point mass M located at the origin. The Newtonian field is given by

$$\boldsymbol{g}_N = -\frac{GM}{r^2}\hat{\boldsymbol{r}}, \tag{A7}$$

and hence the pristine field is given by

$$\boldsymbol{g}_P = -\frac{GM}{r^2}\nu\left(\frac{R_M^2}{r^2}\right)\hat{\boldsymbol{r}}. \tag{A8}$$

Here the MOND radius R_M is given by

$$R_M = \sqrt{\frac{GM}{a_0}}. \tag{A9}$$

From the asymptotic forms of the interpolating function, it follows that the pristine field has the asymptotic behavior

$$\begin{aligned} \boldsymbol{g}_P &\approx -\frac{GM}{r^2}\hat{\boldsymbol{r}} \text{ for } r \ll R_M \\ &\approx -\frac{GM}{R_M}\frac{1}{r}\hat{\boldsymbol{r}} \text{ for } r \gg R_M. \end{aligned} \tag{A10}$$

Since $\boldsymbol{g}_P$ is radial and spherically symmetric, it is also curl free. Hence in this case the quasilinear field $\boldsymbol{g}_Q = \boldsymbol{g}_P$. By computing the divergence of $\boldsymbol{g}_P$ we find that the equivalent dark matter density ρ_{eff} is a spherical halo that surrounds the point mass. The halo is peaked near the MOND radius. For the interpolating function in Equation (A4), there is essentially no mass density for $r < R_M$ but there is a long tail as $r \to \infty$. For $M = M_\odot$ and the value of a_0 quoted above, we find $R_M = 7000$ au, the MOND radius of the Sun.

Finally, we note that we have chosen to use the quasilinear formulation of MOND because of its simplicity. However, essentially equivalent results are obtained by use of the nonlinear formulation of MOND originally introduced by Bekenstein & Milgrom (1984).

Appendix B
Galactic Field Effect on the Solar System

Now let us consider the effect of the galactic gravitational field on the solar system. On the scale of the solar system, the galactic gravitational field can be treated as essentially uniform. Ignoring all solar system objects except the Sun, we must therefore solve

$$\nabla \cdot \boldsymbol{g}_N = -4\pi G M_\odot \delta(\boldsymbol{r}) \quad \text{and} \quad \nabla \times \boldsymbol{g}_N = 0 \tag{B1}$$

subject to the boundary condition $\boldsymbol{g}_N \to \boldsymbol{\gamma}_N$ as $r \to \infty$ where $\boldsymbol{\gamma}_N$ is the constant Newtonian field of the galaxy. The solution is of course

$$\boldsymbol{g}_N = -\frac{GM_\odot}{r^2}\hat{\boldsymbol{r}} + \boldsymbol{\gamma}_N. \tag{B2}$$

In Newtonian gravity, to the extent that the galactic field can be treated as uniform, it has no effect on the relative motion of bodies within the solar system since they all accelerate uniformly in response to it. Tidal effects associated with variation of the galactic field are important only for the most remote solar system objects in the Oort cloud. Remarkably, we

will now show that due to the nonlinearity of the equations, in MOND the galactic field has an effect even on the inner solar system, a phenomenon dubbed "the external field effect" (Famaey et al. 2007; Milgrom 2009; Banik & Zhao 2018a).

To analyze this problem within quasilinear MOND, we make use of Equation (A2) and the product rule to obtain

$$\nabla \cdot \boldsymbol{g}_P = (\nabla \cdot \boldsymbol{g}_N)\nu\left(\frac{g_N}{a_0}\right) + \boldsymbol{g}_N \cdot \nabla\left[\nu\left(\frac{g_N}{a_0}\right)\right] \tag{B3}$$

where $\boldsymbol{g}_N$ is given by Equation (B2). Evidently the first term on the right-hand side is $-4\pi G M_\odot \delta(\boldsymbol{r})$. Using Equation (A5), (A6), and (B3) we obtain

$$\nabla \cdot \boldsymbol{g}_Q = -4\pi G M_\odot \delta(\boldsymbol{r}) - 4\pi G \rho_{\rm ph} \text{ and } \nabla \times \boldsymbol{g}_Q = 0. \tag{B4}$$

Here the phantom mass density $\rho_{\rm ph}$ is defined via

$$-4\pi G \rho_{\rm ph} = \boldsymbol{g}_N \cdot \nabla\left[\nu\left(\frac{g_N}{a_0}\right)\right]. \tag{B5}$$

Equation (B4) must be solved subject to the boundary condition $\boldsymbol{g}_Q \to \boldsymbol{\gamma}_g$ for $r \to \infty$ where $\boldsymbol{\gamma}_g$ is the physical acceleration due to gravity in the solar system due to the galactic field. This is a measurable parameter, and we shall assume that $\boldsymbol{\gamma}_g = \gamma_N \nu(\gamma_N/a_0)$. The latter relation is a very good approximation for disk galaxies that do not have too flat an aspect ratio (Brada & Milgrom 1995; Brown et al. 2018).

In order to analyze the effects of the galactic field on the relative motion of solar system bodies, it is convenient to define the anomalous gravitational field $\boldsymbol{g}_A$ via

$$\boldsymbol{g}_Q = \boldsymbol{g}_A - \frac{GM_\odot}{r^2}\hat{\boldsymbol{r}} + \boldsymbol{\gamma}_g. \tag{B6}$$

$\boldsymbol{g}_A$ captures effects beyond those due to the Newtonian field of the Sun and the uniformly gravitational field of the galaxy. It embodies the external field effect.

It is obvious from Equations (B4) and (B6) that the anomalous field obeys

$$\nabla \cdot \boldsymbol{g}_A = -4\pi G \rho_{\rm ph} \quad \text{and} \quad \nabla \times \boldsymbol{g}_A = 0 \tag{B7}$$

subject to the boundary condition $\boldsymbol{g}_A \to 0$ and $r \to \infty$. In short, $\boldsymbol{g}_A$ is the Newtonian field produced by the phantom mass distribution.

Equations (B2), (B5), and (B7) are the main results of this section. They provide an expression for the phantom mass that sources anomalous effects in the inner solar system. As discussed above, these effects are absent in Newtonian gravity and hence absent in any dark matter model.

The external field effect within the solar system was analyzed by Milgrom within the original nonlinear MOND using a "surrogate mass approximation" (Milgrom 2009). Here we have followed that analysis closely but working within quasilinear MOND. The main difference is that the analysis is simpler for quasilinear MOND, and it can be carried out exactly. This is not entirely by chance: Milgrom constructed quasilinear MOND as a theory for which the surrogate mass approximation would be exact (Milgrom 2010).

Finally for reference we provide a more explicit expression for the phantom mass. It is convenient to work in a system of coordinates wherein the Sun is at the origin and the Galactic center is along the positive z-axis. Then making use of Equations (B2) and (B5), we obtain

$$\rho_{\rm ph} = -\frac{M_\odot}{4\pi R_M^3}\mu(\bar{r}, u) \tag{B8}$$

where we are working in spherical polar coordinates, and $\bar{r} = r/R_M$ and $u = \cos\theta$. The function μ is given by

$$\mu(\bar{r}, u) = \frac{a_0}{g_N}\nu'\left(\frac{g_N}{a_0}\right)\left[\frac{2}{\bar{r}^7} - 4\frac{\gamma_N}{a_0}\frac{u}{\bar{r}^5} + \left(\frac{\gamma_N}{a_0}\right)^2\frac{(3x^2-1)}{\bar{r}^3}\right] \tag{B9}$$

and

$$\frac{g_N}{a_0} = \left[\frac{1}{\bar{r}^4} + \left(\frac{\gamma_N}{a_0}\right)^2 - \frac{2}{\bar{r}^2}\frac{\gamma_N}{a_0}u\right]^{1/2}. \tag{B10}$$

Assuming the interpolating function is given by Equation (A4), the derivative is given by

$$\nu'(x) = -\frac{1}{2\sqrt{x}}\frac{\exp(-\sqrt{x})}{[1-\exp(-\sqrt{x})]^2}. \tag{B11}$$

Equations (B8), (B9), (B10), and (B11) provide the desired explicit expression for $\rho_{\rm ph}$.

To gain some insight into the expressions in the preceding paragraph, we consider some limiting cases. First, let us suppose that $\gamma_N = 0$. In the absence of the galactic field, the expression for the phantom mass simplifies to

$$\rho_{\rm ph} = \frac{M_\odot}{4\pi R_M^3}\frac{1}{\bar{r}^4}\frac{\exp(-1/\bar{r})}{[1-\exp(-1/\bar{r})]^2}. \tag{B12}$$

As expected, the phantom mass distribution is spherically symmetric in the absence of the galactic field. Taking the limit $\bar{r} \to 0$, we find

$$\rho_{\rm ph} \to \frac{M_\odot}{4\pi R_M^3}\left(\frac{R_M}{r}\right)^4 \exp\left(-\frac{R_M}{r}\right); \tag{B13}$$

the phantom mass vanishes exponentially inside the MOND radius. For $\bar{r} \to \infty$

$$\rho_{\rm ph} \to \frac{M_\odot}{4\pi R_M^3}\left(\frac{R_M}{r}\right)^2; \tag{B14}$$

the phantom mass vanishes slowly as a power law far beyond the MOND radius.

Turning to the more relevant case where the galactic field is present, we find that for $\bar{r} \to 0$, the expression in Equation (B13) still holds; the phantom mass vanishes exponentially within the solar system. For $\bar{r} \to \infty$ however, the asymptotic behavior is different. In this limit

$$\rho_{\rm ph} \to \frac{M_\odot}{4\pi R_M^3}\frac{\sqrt{\eta_N}\exp(-\sqrt{\eta_N})}{[1-\exp(-\sqrt{\eta_N})]^2}\left(\frac{R_M}{r}\right)^3 P_2(\cos\theta). \tag{B15}$$

Here for brevity we have written $\gamma_N/a_0 = \eta_N$. Thus, the phantom mass distribution vanishes more quickly as a power law when the galactic field is taken into consideration. In fact, it can be shown that the total phantom mass is finite so long as the external galactic field is present (Milgrom 2010).

The picture that emerges from the asymptotics is that there is essentially no phantom mass in the solar system well within the MOND radius. The phantom mass density must be peaked at

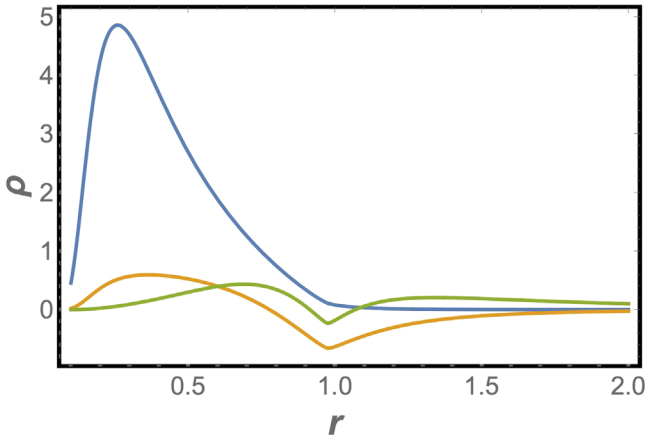

Figure 5. Plot of the phantom density harmonics $\rho_{\mathrm{ph},\ell}$ as a function of distance from the Sun for $\ell = 0$ (blue), $\ell = 1$ (green), and $\ell = 2$ (orange). The density is in units of $M_\odot/R_M^3$ and distance is in units of R_M. In generating these plots, we took $\gamma_g = 1.5a_0$ as discussed in the main text. As expected the mass densities are peaked at a distance of the order of the MOND radius. The origin of the kinks at a common distance from the Sun is discussed in the Appendix text.

around the MOND radius and must decline gradually at greater distances. Moreover, it is clear from the exact expression that ρ_{ph} must be rotationally symmetric about the z-axis. We may therefore expand the phantom mass distribution in harmonics defined via

$$\rho_{\mathrm{ph}\ell}(\bar{r}) = \int_0^\pi d\theta \sin\theta P_\ell(\cos\theta)\rho_{\mathrm{ph}}(\bar{r}, \theta). \tag{B16}$$

These harmonics can be calculated numerically using the exact expression we have deduced for ρ_{ph} above. Figure 5 shows the first few harmonics as a function of r. These plots confirm the general picture that ρ_{ph} is peaked near the MOND radius and exponentially small within it. The plots also reveal a kink at a common value of r in all harmonics.

The origin of the kink is the following. There is a point along the z-axis where the Galactic field and the solar field exactly cancel. This point is known as a saddle point in the literature (Milgrom 1986; Penner 2020; Oria et al. 2021). It is easy to see from Equation (B2) that this distance is $\bar{r} = \sqrt{\eta_N}$. Near this point, the phantom mass diverges and moreover displays an interesting variation in sign depending on the direction from which this point is approached. However, the density has a weak square root divergence at this point and hence there is no substantial mass concentration present here.

In order to calculate the harmonics numerically, we have taken γ_g the galactic gravitational field to be $1.5a_0$ and solved the transcendental equation $\gamma_g = \gamma_N \nu(\gamma_N/a_0)$ to obtain $\gamma_N = 0.9a_0$. The results are not sensitive to the particular value of γ_g/a_0 so long as it is a factor of order unity. The value we have used is based on the rotation curve model of the Milky Way described in McGaugh (2018). It is also compatible with the value $\gamma_g = (1.9 \pm 0.1)a_0$ obtained from Gaia astrometry (Klioner et al. 2021).

Appendix C
Multipole Expansion in Gravity

The Newtonian gravitational potential ψ_N is defined via the relation $\boldsymbol{g}_N = -\nabla\psi_N$. For a mass distribution ρ, the potential is given by the exact expression

$$\psi_N(\boldsymbol{r}) = -\int d\boldsymbol{r}' \frac{G\rho(\boldsymbol{r}')}{|\boldsymbol{r} - \boldsymbol{r}'|}. \tag{C1}$$

It is useful to recall the expansion (Matthews & Walker 1970)

$$\frac{1}{|\boldsymbol{r} - \boldsymbol{r}'|} = \sum_{\ell=0}^{\infty}\sum_{m=-\ell}^{+\ell} \frac{4\pi}{(2\ell+1)} \frac{r_<^\ell}{r_>^{(\ell+1)}} Y_{\ell m}^*(\theta', \phi') Y_{\ell m}(\theta, \phi) \tag{C2}$$

where $r_<$ denotes the lesser of r and r', and $r_>$ denotes the greater.

For the circumstance that the mass distribution is localized near the origin, and the observation point lies outside of the support of the mass distribution, by use of Equations (C1) and (C2), we obtain

$$\psi_N(\boldsymbol{r}) = -\frac{GM}{R}\sum_{\ell=0}^{\infty}\sum_{m=-\ell}^{\ell} J_{\ell m}\left(\frac{R}{r}\right)^{\ell+1}\sqrt{\frac{4\pi}{2\ell+1}}Y_{\ell m}(\theta, \phi). \tag{C3}$$

Here M is the mass scale of the mass distribution, R is the size scale, and the dimensionless multipole moments $J_{\ell m}$ are given by

$$J_{\ell m} = \frac{1}{MR^\ell}\int d\boldsymbol{r}\sqrt{\frac{4\pi}{2\ell+1}} r^\ell Y_{\ell m}^*(\theta, \phi)\rho(\boldsymbol{r}). \tag{C4}$$

This is the usual multipole expansion familiar from electrostatics: it corresponds to the situation that the mass distribution is localized and the field is desired at a point far from the mass distribution. As usual, the (ℓ, m) term in the field falls off with distance as $1/r^{\ell+1}$ and has an angular dependence given by $Y_{\ell m}(\theta, \phi)$.

Here we are interested in the complementary situation that within the mass distribution there is an empty cavity devoid of mass. We are interested in the field near the center of this cavity. Making use of Equations (C1) and (C2), we obtain the complementary multipole expansion

$$\psi_N(\boldsymbol{r}) = -\frac{GM}{R}\sum_{\ell=0}^{\infty}\sum_{-\ell}^{\ell} \mathcal{J}_{\ell m}\left(\frac{r}{R}\right)^{\ell}\sqrt{\frac{4\pi}{2\ell+1}}Y_{\ell m}(\theta\phi). \tag{C5}$$

Again, M is the mass scale of the mass distribution, and R the size scale. The dimensionless complementary multipole moments $\mathcal{J}_{\ell m}$ are given by

$$\mathcal{J}_{\ell m} = \frac{R^{\ell+1}}{M}\sqrt{\frac{4\pi}{2\ell+1}}\int d\boldsymbol{r}\frac{1}{r^{\ell+1}}Y_{\ell m}^*(\theta, \phi)\rho(\boldsymbol{r}). \tag{C6}$$

In contrast to the usual multipole expansion, we see that here the (ℓ, m) term in the expansion grows as r^ℓ; its angular dependence is still given by $Y_{\ell m}(\theta, \phi)$.

For the special case of cylindrical symmetry, $\mathcal{J}_{\ell m} = 0$ except for $m = 0$. Hence, the complementary multipole expansion simplifies to

$$\psi_N(\boldsymbol{r}) = -\frac{GM}{R}\sum_{\ell=0}^{\infty}\mathcal{J}_{\ell 0}\left(\frac{r}{R}\right)^{\ell}P_\ell(\cos\theta), \tag{C7}$$

and the nonvanishing multipole moments are given by

$$\mathcal{J}_{\ell 0} = \frac{R^{\ell+1}}{M}\int d\boldsymbol{r}\frac{1}{r^{\ell+1}}P_\ell(\cos\theta)\rho(\boldsymbol{r}). \tag{C8}$$

For reference, it is useful to explicitly write the quadrupole term for the case of cylindrical symmetry

$$\psi_N^Q(\boldsymbol{r}) = -\frac{GM}{R^3}\mathcal{J}_{20}r^2P_2(\cos\theta) \tag{C9}$$

where

$$\mathcal{J}_{20} = \frac{R^3}{M}\int d\boldsymbol{r}\frac{1}{r^3}P_2(\cos\theta)\rho(\boldsymbol{r}). \tag{C10}$$

Thus far in our discussion, we have focused on the multipole expansion for the Newtonian gravitational field $\boldsymbol{g}_N = -\nabla\psi_N$. However the same discussion applies, mutatis mutandis, for the MOND external field $\boldsymbol{g}_A = -\nabla\psi_A$, which is mathematically the Newtonian field produced by the phantom mass $\rho_{\rm ph}$.

We now evaluate the quadrupole term in the multipole expansion of Equation (C5) for several cases of interest. The simplest mass distribution that produces a quadrupolar field is two point masses each of mass M located on the z-axis symmetrically about the origin at a distance $2R$ from each other. This distribution has cylindrical symmetry, and a simple calculation using Equation (C10) reveals that $\mathcal{J}_{20} = 2$ in this case. Note that the multipole moment is positive here. This is called a prolate quadrupole.

Next consider a circle of radius R and total mass M that lies in the x–y plane centered about the origin. This distribution also has cylindrical symmetry and in this case, use of Equation (C10) reveals that $\mathcal{J}_{20} = -\frac{1}{2}$ here. Note that the multipole moment is negative here. This is called an oblate quadrupole.

Next let us consider the quadrupolar field of a hypothetical Planet Nine. In the secular approximation, we want the orbit-averaged field of Planet Nine. In other words, we assume that the mass of Planet Nine is distributed nonuniformly over the ellipse corresponding to its orbit. The amount of mass contained in any arc of the orbit is proportional to the time it takes Planet Nine to traverse that arc. We assume that the orbit lies in the x–y plane with the Sun at the origin and the point of perihelion on the positive x-axis. Note that this mass distribution does not have cylindrical symmetry. Nonetheless, we find upon explicit evaluation that $\mathcal{J}_{2m} = 0$ except for $m = 0$. For that case, setting $M \to m_9$ and $R \to a_9$, where m_9 is the mass of Planet Nine and a_9 is the semimajor axis of its orbit, we obtain

$$\mathcal{J}_{20} = -\frac{1}{2}\frac{1}{(1-e_9^2)^{3/2}} \tag{C11}$$

where e_9 is the eccentricity of the orbit of Planet Nine. Note that Equation (C11) reduces to the expected result for a circle when $e_9 = 0$. It follows from Equation (C5) that the quadrupolar field of Planet Nine is cylindrically symmetric and given by

$$\psi_9^Q(\boldsymbol{r}) = \frac{1}{2}\frac{Gm_9}{a_9^3}\frac{1}{(1-e_9^2)^{3/2}}r^2P_2(\cos\theta). \tag{C12}$$

We postpone for now the derivation of the multipole moments $\mathcal{J}_{2m}$ for the orbit of Planet Nine quoted above, but we note that the emergent cylindrical symmetry in the moments is analogous to the well-known fact that the moment of inertia of a cube is isotropic and diagonal. A cube is by no means spherically symmetrical, but it has sufficient symmetry to render the moment of inertia isotropic.

We note that the dominant interaction of Planet Nine with objects in the inner solar system is via its quadrupole field. The reader may have noticed that the orbit-averaged mass distribution has a nonzero dipole moment, but it is well known that in an inertial frame centered at the Sun, the dipole interaction term is exactly canceled by the "indirect interaction" potential (see, for example, Murray & Dermott 2000).

We turn now to the multipole expansion of the anomalous field in MOND. The phantom mass distribution is cylindrically symmetric about the z-axis, which is taken to point toward the Galactic center, with the Sun at the origin. The nonvanishing multipole moments are written as $\mathcal{J}_{\ell 0} = q_\ell/4\pi$ where

$$q_\ell = -2\pi\int_0^\infty d\bar{r}\int_{-1}^{+1} du\bar{r}^{1-\ell}P_\ell(u)\mu(\bar{r}, u) \tag{C13}$$

where $\mu(\bar{r}, u)$ is given by Equation (B9). If we choose the Galactic field $\gamma_g/a_0 = 1.5$ as in the previous section, then we find by numerical evaluation of Equation (C13) the following values for the lowest-order multipoles:

$$q_1 \approx 0, \quad q_2 = 1.00, \quad q_3 = 0.51\ldots \tag{C14}$$

That $q_1 \approx 10^{-12}$ in our numerical evaluation is encouraging, since it is known that $q_1 = 0$ exactly for the phantom mass. This was shown by Bekenstein & Milgrom (1984) and Milgrom (2009). Thus for MOND, as for Planet Nine, its dominant interaction with bodies in the inner solar system is quadrupolar. We note that the values of q_2 and q_3 are functions of the dimensionless quantity γ_g/a_0 and are also sensitive to the form of the interpolating function (this sensitivity is studied by Milgrom 2009). Thus at the present stage of development, MOND is not able to pin down the precise values of these parameters. The takeaway from our computation and the tabulation by Milgrom (2009) is that q_2 and q_3 are of order unity to within an order of magnitude or two. Studies of the outer solar system will help constrain the values of these parameters and hence the interpolating function in a way that is independent of and complementary to traditional studies of galaxy rotation (McGaugh et al. 2016). The parameter q_2 is also bounded by spacecraft orbits. The best bounds are from Cassini (Hees et al. 2014). Our parameter q_2 is related to the parameter Q_2 in Hees et al. (2014) via

$$q_2 = \frac{4\pi}{3}\sqrt{\frac{GM_{\rm sun}}{a_0^3}}\,Q_2. \tag{C15}$$

$q_2 = 1.00$ corresponds to $Q_2 = 27\times10^{-27}$ s^{-2}, which is in tension with the Cassini bound of $(3\pm3)\times10^{-27}$ s^{-2} (Hees et al. 2014). However, Hees et al. (2016) showed that other interpolating functions yield values of Q_2 that are compatible with the Cassini bound. Our results on orbital dynamics are not sensitive to the form of the interpolating function, and a quadrupole compatible with the Cassini bound is sufficient for our purpose.

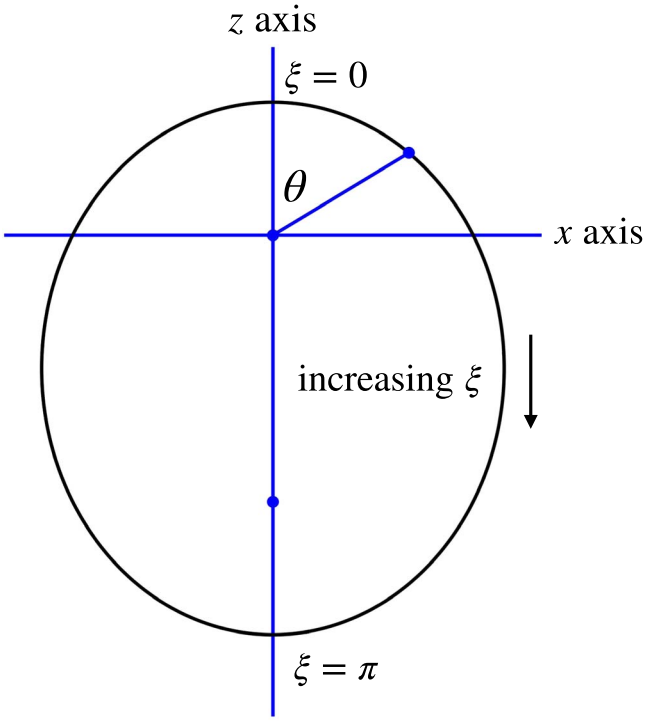

Figure 6. The orbit of Planet Nine is taken to lie in the z–x plane with the Sun at the origin. The perihelion is assumed to lie on the positive z-axis. The multipole moments for this reference configuration are denoted $J^{(0)}$ and $\mathcal{J}^{(0)}$. The eccentric anomaly ξ is taken to be zero at perihelion and to increase clockwise in the figure. Also shown in the figure is the angle θ for an arbitrary point on the orbit. θ is the spherical polar colatitude of that point, and it also represents the true anomaly around the orbit.

For reference, we now provide an explicit expression for the quadrupole field in MOND

$$\psi_A^Q = -\frac{GM_\odot}{R_M^3}\frac{q_2}{4\pi}r^2 P_2(\cos\theta). \tag{C16}$$

Equations (C12) and (C16) provide expressions for the quadrupolar fields that are used in the paper to compare the order of magnitude of the MOND perturbation with that of Planet Nine on objects in the Kuiper Belt. Note that the MOND potential has a spurious reflection symmetry about the x–y plane in the quadrupole approximation. This symmetry is absent in the problem since there is difference between the direction pointing toward Galactic center and the direction pointing away from it. The octupole term breaks this symmetry, and inclusion of this term will prove important for our analysis below. The multipole expansion is a good approximation for $r \ll R_M = 7000$ au. For a KBO whose orbit extends to 500 au, this condition is reasonably well satisfied.

For later use, let us also calculate the orbit-averaged multipole moments for Planet Nine. We take the orbit to lie in the z–x plane with the Sun at the origin and the perihelion along the positive z-axis. The ellipse may then be described parametrically by the equations

$$z = a_9(\cos\xi - e_9) \quad \text{and} \quad x = a_9\sqrt{1-e_9^2}\,\sin\xi. \tag{C17}$$

Here the parameter ξ is known as the eccentric anomaly and ranges from 0–2π around the ellipse (see Figure 6). It is useful to also calculate the spherical polar coordinates (r, θ, ϕ) of points around the ellipse as a function of ξ. It follows from Equation (C17) that

$$r = a_9(1 - e_9\cos\xi) \tag{C18}$$

and that

$$\cos\theta = \frac{\cos\xi - e_9}{1 - e_9\cos\xi} \quad \text{and} \quad \sin\theta = \frac{\sqrt{1-e_9^2}\,\sin\xi}{1 - e_9\cos\xi}. \tag{C19}$$

Finally $\phi = 0$ for $0 < \xi < \pi$ and $\phi = \pi$ for $\pi < \xi < 2\pi$. Let us assume that the planet starts at $\xi = 0$ at $t = 0$ and moves in the direction of increasing ξ. The anomaly ξ of the planet at time t is then given by Kepler's anomaly equation

$$\frac{2\pi t}{T_9} = \xi - e_9\sin\xi \;\Leftrightarrow\; \frac{2\pi}{T_9}\frac{dt}{d\xi} = 1 - e_9\cos\xi. \tag{C20}$$

Here T_9 denotes the orbital period of Planet Nine. The mass dm associated with an infinitesimal arc of the orbit is proportional to the time it takes to traverse the arc. Hence, $dm/m_9 = dt/T_9$ and making use of Equation (C20), we then obtain

$$\frac{dm}{d\xi} = \frac{m_9}{2\pi}(1 - e_9\cos\xi). \tag{C21}$$

We are now in a position to compute the orbit-averaged multipole moments. We find that for even m

$$J_{\ell m}^{(0)} = \frac{1}{\pi}\sqrt{\frac{(\ell-m)!}{(\ell+m)!}}\int_0^\pi d\xi(1 - e_9\cos\xi)^{\ell+1}P_{\ell,m} \times\left(\frac{\cos\xi - e_9}{1 - e_9\cos\xi}\right) \tag{C22}$$

and for odd m $J_{\ell m}^{(0)} = 0$. The superscript in $J^{(0)}$ is meant to remind us that this multipole moment is computed with the orbit in the z–x plane with the Sun at the origin and the perihelion along the positive z-axis. Equation (C22) was obtained from Equation (C4) by making the following substitutions. $M \to m_9$, $R \to a_9$, and $d\boldsymbol{r}\rho \to d\xi(dm_9/d\xi)$, using Equation (C21) for $dm/d\xi$, Equation (C18) for r and Equation (C19) for $\cos\theta$. It is also helpful to recall that

$$Y_{\ell,m}(\theta,\phi) = \sqrt{\frac{2\ell+1}{4\pi}}\sqrt{\frac{(\ell-m)!}{(\ell+m)!}}P_{\ell m}(\cos\theta)e^{im\phi}. \tag{C23}$$

The integral in Equation (C22) is evaluated only over the right half of the orbit ($0 < \xi < \pi$) for which $e^{im\phi} = 1$. For the left half ($\pi < \xi < 2\pi$), the quantity $e^{im\phi} = (-1)^m$. Hence the contribution of the right half must be doubled for even m, and for odd m the two halves cancel leading to $J_{\ell m}^{(0)} = 0$.

For the record, we explicitly provide the low-order multipoles that are most relevant to our analysis. We find upon integrating Equation (C22) that $J_{0,0}^{(0)} = 1$. The nonzero quadrupole moments are found to be

$$J_{2,\pm2}^{(0)} = \frac{1}{4}\sqrt{\frac{3}{2}}(1 - e_9^2) \quad \text{and} \quad J_{2,0}^{(0)} = \frac{1}{4}(1 + 9e_9^2). \tag{C24}$$

The nonzero octupole moments are found to be

$$J^{(0)}_{3,\pm 2} = -\frac{5}{16}\sqrt{\frac{15}{2}}\, e_9(1 - e_9^2) \quad \text{and}$$
$$J^{(0)}_{3,0} = -\frac{5}{16} e_9(3 + 11 e_9^2). \tag{C25}$$

Obviously, the same expressions would apply for a KBO with the replacement $e_9 \to e_K$ where e_K is the eccentricity of the KBO or for Neptune with the replacement $e_9 \to e_8$ where e_8 is the eccentricity of the orbit of Neptune.

The complementary multipole moments $\mathcal{J}^{(0)}_{\ell m}$ may be calculated similarly using Equation (C6). Analogous to Equation (C22), we obtain

$$\mathcal{J}^{(0)}_{\ell m} = \frac{1}{\pi}\sqrt{\frac{(\ell - m)!}{(\ell + m)!}} \int_0^\pi d\xi \frac{1}{(1 - e_9 \cos\xi)^\ell} P_{\ell m} \times \left(\frac{\cos\xi - e_9}{1 - e_9\cos\xi}\right). \tag{C26}$$

For later use, we provide low-order complementary multipole moments that will be especially relevant. By explicit evaluation of the integral in Equation (C26), we find $\mathcal{J}^{(0)}_{00} = 1$. The complementary quadrupole moments are

$$\mathcal{J}^{(0)}_{2,\pm 2} = \frac{1}{4}\sqrt{\frac{3}{2}}\frac{1}{(1 - e_9^2)^{3/2}} \quad \text{and} \quad \mathcal{J}^{(0)}_{2,0} = \frac{1}{4}\frac{1}{(1 - e_9^2)^{3/2}}. \tag{C27}$$

Note that Equation (C27) does not match Equation (C11) because they are computed for different orientations of the orbit. We describe in the next section how to obtain Equation (C11) from Equation (C27).

Appendix D
The Disturbing Function

As a prelude, consider two distributions of mass: ρ_1 localized near the origin and ρ_2 located far from the origin. The gravitational potential energy of these two distributions is

$$\mathcal{R} = -G\int d\boldsymbol{r}\int d\boldsymbol{r}'\, \frac{\rho_1(\boldsymbol{r}')\rho_2(\boldsymbol{r})}{|\boldsymbol{r} - \boldsymbol{r}'|} = \int d\boldsymbol{r}\psi_1(\boldsymbol{r})\rho_2(\boldsymbol{r}). \tag{D1}$$

Here ψ_1 denotes the gravitational potential due to ρ_1. Making use of the multipole expansion Equation (C3) and the definition of complementary moments Equation (C6), we obtain

$$\mathcal{R} = -\frac{GM_1M_2}{R_2}\sum_{\ell=0}^{\infty}\sum_{m=-\ell}^{\ell}\left(\frac{R_1}{R_2}\right)^\ell \mathcal{J}^*_{\ell m} J_{\ell m}. \tag{D2}$$

Here M_1 is the mass scale for the distribution ρ_1, and R_1 is the length scale. M_2 and R_2 are the corresponding quantities for ρ_2. If we regard $J_{\ell m}$ as the $2\ell + 1$ components of a column vector J_ℓ and $\mathcal{J}^*_{\ell m}$ as the components of a row vector $\mathcal{J}^\dagger_\ell$, we may write Equation (D2) more compactly as

$$\mathcal{R} = -\frac{GM_1M_2}{R_2}\sum_{\ell=0}^{\infty}\left(\frac{R_1}{R_2}\right)^\ell \mathcal{J}^\dagger_\ell J_\ell. \tag{D3}$$

Now let us consider the effect of the MOND field $\boldsymbol{g}_A$ on the motion of a KBO. Under the influence of the Sun alone, the KBO would trace an ellipse in accordance with Kepler's laws. The ellipse is characterized by five orbital elements (a_K, e_K, ω_K, i_K, and Ω_K). The semimajor axis a_K and the eccentricity e_K specify the shape of the orbit. The Euler angles (ω_K, i_K, Ω_K) specify the orientation and will be defined more precisely momentarily. Under the influence of perturbations, the orbital elements change slowly. In the secular approximation, the semimajor axis does not change, and the dynamics is controlled by the disturbing function $\mathcal{R}$, which is the potential energy of the KBO time averaged over its Keplerian orbit in the perturbing MOND potential (Moulton 1984; Murray & Dermott 2000).

The disturbing function is often calculated in an expansion in the eccentricity of the orbit or the inclination of the orbit (Murray & Dermott 2000). In our problem, we need the disturbing function for arbitrary eccentricity and inclination, and hence we cannot use expansions in these variables. We have developed a method to calculate the secular disturbing function by expanding it in a multipole expansion and computing the quadrupole and octupole terms exactly. In principle, the higher multipoles can also be calculated by this method but they are not needed for our immediate purpose.

The key ingredient in our approach is to recognize that the multipole moments J_ℓ and $\mathcal{J}_\ell$ transform as rank ℓ tensors under rotations. Thus if, for example, a mass distribution ρ is rotated about the y-axis by an angle φ, then the multipole moments transform as $J_\ell \to R^{(\ell)}_y(\varphi)J_\ell$ and similarly for $\mathcal{J}_\ell$. Here $R^{(\ell)}_y(\varphi)$ is a $(2\ell+1)\times(2\ell+1)$ dimensional unitary matrix that corresponds to the rotation about the y-axis for a rank ℓ tensor. We will discuss the form of these matrices shortly, but first let us use them to develop an expression for the disturbing function.

In this section we will find it convenient to work in a coordinate frame wherein the Sun is at the origin, and the y-axis points in the direction of the galactic center. The multipole moments of the phantom mass distribution are then given by

$$\mathcal{J}_\ell = R^{(\ell)}_x\left(-\frac{\pi}{2}\right)\mathcal{J}^{(0)}_\ell \tag{D4}$$

where $R^{(\ell)}_x(-\pi/2)$ denotes the matrix corresponding to a rotation about the x-axis by $-\pi/2$ and

$$\mathcal{J}^{(0)}_{\ell m} = \frac{q_\ell}{4\pi}\delta_{m,0} \tag{D5}$$

are the multipole moments for the phantom mass distribution when the Galactic center is taken to be along the z-axis, as it was in the preceding section. q_ℓ is given by Equations (C13) and (C14). We will compute the components of $\mathcal{J}_\ell$ below explicitly for $\ell = 2$ and $\ell = 3$.

The z–x plane will be used as the reference plane to describe the evolution of the KBO orbit. We take as the reference orientation the configuration such that the KBO orbit lies in the reference plane with its perihelion located on the positive z-axis. The orbital elements (ω_K, i_K, Ω_K) correspond to the orientation obtained by first rotating the reference orbit about the y-axis by the angle ω_K, then about the z-axis by the angle i_K and finally about the y-axis again by an angle Ω_K. The orbit orientation is also fully specified by two unit vectors: the apsidal vector $\hat{\boldsymbol{a}}_K$, which points from the Sun to the direction of the perihelion, and the orbit normal $\hat{\boldsymbol{n}}_K$, which is normal to the plane of the orbit and points in the direction of the angular momentum of the KBO. In the reference configuration, $\hat{\boldsymbol{a}}^{(0)}_K = \hat{\boldsymbol{z}}$ and $\hat{\boldsymbol{n}}^{(0)}_K = \hat{\boldsymbol{y}}$. The reader may find it helpful to

visualize how $\hat{\boldsymbol{a}}_K$ and $\hat{\boldsymbol{n}}_K$ change as the orbit undergoes successive y–z–y rotations by the angles $(\omega_K, i_K, \Omega_K)$. Note in particular that $\hat{\boldsymbol{n}}_K$ will be inclined at an angle i_K to the positive y-axis at the end of the process. The orbit-averaged multipole moments of the KBO with orbital elements (a_K, e_K, ω_K, i_K, and Ω_K) are given by

$$J_\ell = R_y^{(\ell)}(\Omega) R_z^{(\ell)}(i_K) R_y^{(\ell)}(\omega_K) J_\ell^{(0)} \tag{D6}$$

where $J_\ell^{(0)}$ denotes the moments for the standard orientation of the orbit that we calculated in the preceding section. (See Equations (C22), (C24), and (C25) with the replacement $e_9 \to e_K$.)

We can now write an exact formal expression for the disturbing function that governs the evolution of the KBO orbit under the influence of the MOND field. We substitute in Equation (D3) the expression for $\mathcal{J}_\ell$ given in Equation (D4) and the expression for $\mathcal{J}_\ell$ given in Equation (D6) to obtain

$$\mathcal{R} = -\frac{G m_K M_\odot}{R_M} \sum_{\ell=2}^{\infty} \left(\frac{a_K}{R_M}\right)^\ell \mathcal{M}_\ell \tag{D7}$$

where the matrix element $\mathcal{M}_\ell$ is given by

$$\mathcal{M}_\ell = \mathcal{J}_\ell^\dagger R_y^{(\ell)}(\Omega_K) R_z^{(\ell)}(i_K) R_y^{(\ell)}(\omega_K) J_\ell^{(0)}. \tag{D8}$$

$\mathcal{M}_\ell$ depends on e_K through $J_\ell^{(0)}$ and on $(\omega_K, i_K, \Omega_K)$ through the rotation factors. It also depends on q_ℓ through $\mathcal{J}_\ell$. Note that we have omitted the $\ell = 0$ term because it is independent of all of the orbital elements and therefore does not have any effect on the dynamics. We are able to omit the $\ell = 1$ term because the phantom mass has no dipole moment. Intuitively we expect that due to the cylindrical symmetry of the MOND field about the y-axis, the matrix element $\mathcal{M}$ and the disturbing function should be independent of Ω_K. Mathematically this happens because $\mathcal{J}_\ell$ in Equation (D4) proves to be invariant under rotations about the y-axis. Thus $R_y^{(\ell)}(\varphi)\mathcal{J}_\ell = \mathcal{J}_\ell$ for any angle φ, which implies $\mathcal{J}_\ell^\dagger R_y^{(\ell)}(\Omega_K) = \mathcal{J}_\ell^\dagger$.

We may write the rotation matrix $R_y^{(\ell)}(\varphi) = \exp[-iL_y^{(\ell)}\varphi]$ where $L_y^{(\ell)}$ is the $(2\ell+1)\times(2\ell+1)$ matrix corresponding to the generator of rotations about the y-axis. From the general theory of representations of the rotation group (familiar to physicists as the quantum theory of angular momentum), we know that $L_y^{(\ell)}$ has $2\ell+1$ eigenvectors $v_{\ell\mu}^{(y)}$ with eigenvalue μ, where μ is an integer in the range $-\ell \leqslant \mu \leqslant \ell$. In terms of these eigenvectors, $R_y^{(\ell)}(\varphi)$ has the spectral representation

$$R_y^{(\ell)}(\varphi) = \sum_{\mu=-\ell}^{\ell} \exp(-i\mu\varphi) v_{\ell\mu}^{(y)} v_{\ell\mu}^{(y)\dagger}. \tag{D9}$$

Note that $v_{\ell\mu}^{(y)}$ is a $2\ell+1$ component column vector; $v_{\ell\mu}^{(y)\dagger}$ is a $2\ell+1$ component row vector. Hence, the right-hand side of Equation (D9) is a $(2\ell+1)\times(2\ell+1)$ matrix, as it should be. Sometimes, we will find it convenient to explicitly write the components of $v_{\ell\mu}^{(y)}$ as $v_{\ell\mu}^{(y)}(m)$ where m is an integer in the range $-\ell \leqslant m \leqslant \ell$. Similarly, we may write the spectral representation

$$R_x^{(\ell)}(\varphi) = \sum_{\mu=-\ell}^{\ell} \exp(-i\mu\varphi) v_{\ell\mu}^{(x)} v_{\ell\mu}^{(x)\dagger} \tag{D10}$$

where $v_{\ell\mu}^{(x)}$ are eigenvectors of $L_x^{(\ell)}$, the generator of rotations about the x-axis. We are working in a basis wherein $L_z^{(\ell)}$ is diagonal. Hence, the eigenvectors are $v_{\ell\mu}^{(z)}(m) = \delta_{\mu,m}$, and the matrix $R_z^{(\ell)}(\varphi)$ is diagonal. Its effect on a vector is simply to multiply each component of the vector by the appropriate phase. Thus,

$$R_z^{(\ell)}(\varphi) J_\ell \to \exp(-im\varphi) J_{\ell m}. \tag{D11}$$

With the help of these results, we arrive at the following expression for the matrix element $\mathcal{M}_\ell$ in Equation (D12):

$$\mathcal{M}_\ell = \sum_{\mu\mu'} e^{-i\mu\Omega_K} [\mathcal{J}_\ell^\dagger v_{\ell\mu}^{(y)}] \mathcal{I}_{\mu\mu'} [v_{\ell\mu'}^{(y)\dagger} J_\ell^{(0)}] e^{-i\mu'\omega_K} \tag{D12}$$

where the sums over μ and μ' range from $-\ell$ to ℓ, and the inclination factor $\mathcal{I}$ is given by

$$\begin{aligned}\mathcal{I}_{\mu\mu'} &= \sum_{\mu''=\ell}^{\ell} [v_{\ell\mu}^{(y)\dagger} v_{\ell\mu''}^{(z)}] \exp(-i\mu'' i_K) [v_{\ell\mu''}^{(z)\dagger} v_{\ell\mu'}^{(y)}] \\ &= \sum_{\mu''=-\ell}^{\ell} v_{\ell\mu}^{(y)}(\mu'') \exp(-i\mu'' i_K) v_{\ell\mu'}^{(y)}(\mu'').\end{aligned} \tag{D13}$$

Equations (D12) and (D13) provide the tools needed to calculate the matrix element $\mathcal{M}_\ell$ and hence the disturbing function. We illustrate the computation for $\ell = 2$ and also carry it out explicitly for $\ell = 3$ since we need the disturbing function to octupole order for our analysis. However, we note that closed-form expressions for $v_{\ell\mu}^{(y)}$, $\mathcal{J}_\ell$, and $J_\ell^{(0)}$ exist for arbitrary ℓ and hence the procedure outlined above allows us to compute the matrix element for any ℓ exactly without perturbing in e_K or i_K.

To obtain $\mathcal{M}_2$, our first task is to compute $\mathcal{J}_2$ for the phantom mass distribution. Using the spectral representation for $R_x(-\pi/2)$, we may write Equation (D4) as

$$\mathcal{J}_2 = \sum_{\mu=-2}^{2} v_{2\mu}^{(x)} [v_{2\mu}^{(x)\dagger} \mathcal{J}_2^{(0)}]. \tag{D14}$$

Making use of the explicit formulae for $v_{2\mu}^{(x)}$ tabulated below and Equation (D5) for $\mathcal{J}_2^{(0)}$, we obtain

$$v_{2,\pm2}^{(x)\dagger} \mathcal{J}_2^{(0)} = \frac{q_2}{4\pi}\frac{\sqrt{6}}{4} \text{ and } v_{2,0}^{(x)\dagger} \mathcal{J}_2^{(0)} = \frac{q_2}{4\pi}\frac{1}{2}. \tag{D15}$$

Equations (D14) and (D15) yield

$$\mathcal{J}_2 = -\frac{q_2}{4\pi}\begin{bmatrix}\sqrt{3/8}\\ 0\\ 1/2\\ 0\\ \sqrt{3/8}\end{bmatrix} = -\frac{q_2}{4\pi} v_{2,0}^{(y)}. \tag{D16}$$

The last equality above shows that $\mathcal{J}_2$ is proportional to the eigenvector of $L_y^{(2)}$ that is invariant under rotations about the y-axis.

We now compute the ingredients that make up the matrix element $\mathcal{M}_2$ given by Equation (D12). From Equation (D16), it follows that

$$\mathcal{J}_2^\dagger v_{2\mu}^{(y)} = -\frac{q_2}{4\pi} \tag{D17}$$

for $\mu = 0$ and zero for other values of μ. Using Equation (C24) for $J_2^{(0)}$ and the eigenvectors $v_{2\mu}^{(y)}$ tabulated below, we find

$$v_{2,\pm 2}^{(y)\dagger} J_2^{(0)} = -\frac{5\sqrt{6}}{8} e_K^2,$$
$$v_{2,0}^{(y)\dagger} J_2^{(0)} = \frac{1}{8}(4 + 6e_K^2). \tag{D18}$$

Making use of the tabulated eigenvectors and Equation (D13), we can also compute the relevant components of the inclination factor

$$\mathcal{I}_{0,\pm 2} = \frac{1}{4}\sqrt{\frac{3}{2}}[\cos(2i_K) - 1],$$
$$\mathcal{I}_{0,0} = \frac{1}{4} + \frac{3}{4}\cos(2i_K). \tag{D19}$$

Combining the results in Equations (D17), (D18), and (D19) in accordance with Equations (D7) and (D12), we finally obtain the $\ell = 2$ or quadrupole term in the disturbing function

$$\mathcal{R}_Q = \frac{G m_K M_\odot}{R_M}\left(\frac{a_K}{R_M}\right)^2 \frac{q_2}{32\pi}\mathcal{S}_Q \tag{D20}$$

with

$$\mathcal{S}_Q = -2 - 3e_K^2 + 15e_K^2\cos(2\omega_K) + 6\cos^2 i_K + 9e_K^2\cos^2 i_K - 15e_K^2\cos(2\omega_K)\cos^2 i_K. \tag{D21}$$

Equations (D20) and (D21) are the key formulae in this section.

We now briefly consider the disturbing function that describes the effect of Planet Nine on the dynamics of a KBO in the quadrupole approximation. We assume that the orbit of Planet Nine lies in the z–x plane with the Sun at the focus, and the perihelion on the positive z-axis. We use the z–x plane as the reference plane and assume that the orbit of Planet Nine remains fixed for the time duration of interest. The reference configuration of the KBO orbit is one wherein it lies in the reference plane with the perihelion along the positive z-axis. The configuration (ω_K, i_K, Ω_K) corresponds to giving the orbit a y–z–y sequence of rotations by the angles ω_K, i_K, and Ω_K, respectively. Hence, the quadrupolar disturbing function is given by the $\ell = 2$ term in Equation (D7) with the replacements $M_\odot \to m_9$ and $R_M \to a_9$. $\mathcal{M}_2$ is given by Equation (D8) with $J_2^{(0)}$ still given by Equation (C24) but with $\mathcal{J}_2$ given by Equation (C27) not by Equation (D16). Comparing Equation (C27) to Equation (D16), we see that the only change in $\mathcal{M}_2$ is the replacement

$$\frac{q_2}{4\pi} \to -\frac{1}{2}\frac{1}{(1 - e_9^2)^{3/2}}. \tag{D22}$$

Hence, the disturbing function for Planet Nine acting on the KBO to quadrupole order is given by making the same replacement in Equation (D20) leading to

$$\mathcal{R}_Q^{(9)} = -\frac{G m_K m_9}{a_9}\left(\frac{a_K}{a_9}\right)^2 \frac{1}{16}\frac{1}{(1 - e_9^2)^{3/2}}\mathcal{S}_Q. \tag{D23}$$

Here, $\mathcal{S}_Q$ is still given by Equation (D21).

On long timescales, it is not valid to treat the orbit of Planet Nine as fixed. It should evolve slowly in response to perturbations by the four known giant planets. In the analysis of the interaction of Planet Nine and a KBO, it is therefore better to use a fixed plane such as the mean ecliptic as the reference plane rather than the orbital plane of Planet Nine as we have done above. The disturbing function would then be a function of the orbital elements of both the KBO and Planet Nine. We have derived such expressions for the disturbing function to quadrupole and octupole order, and in principle, the expressions can be extended to arbitrary orders using our computational scheme. We will present this analysis elsewhere since we do not need these expressions for our present purpose. Similar expressions have been obtained by Mardling (2010) but are not available in the literature.

Another useful variation of Equation (D23) to consider is the disturbing function that describes the effect of Neptune or one of the other giant planets on the motion of a KBO in the secular approximation. The same expression applies as for the interaction of a KBO with Planet Nine but with the following replacements in Equations (D23) and (D21): (m_K, a_K, e_K) $\to$ (m_8, a_8, e_8) and (m_9, a_9, e_9) $\to$ (m_K, a_K, e_K) since Neptune replaces the KBO as the object in the inner orbit, and the KBO replaces Planet Nine as the outer object. Bearing in mind that, to a good approximation, the giant planets have essentially circular orbits in a common plane, their combined effect on a KBO to quadrupole order is described by the following well-known approximate disturbing function:

$$\mathcal{R}_Q^{(\mathrm{G})} = \frac{G m_K}{a_K^3}\frac{1}{8}\frac{(1 - 3\cos^2 i_K)}{(1 - e_K^2)^{3/2}}\sum_{i=5,6,7,8} m_i a_i^2. \tag{D24}$$

Now let us return to the disturbing function that describes the effect of the galactic field on a KBO in MOND and work out the $\ell = 3$ octupole term in Equation (D7). The derivation is similar to that of the quadrupole, and for the sake of brevity we only provide the final result

$$\mathcal{R}_{\mathrm{oct}} = -\frac{G m_K M_\odot}{R_M}\left(\frac{a_K}{R_M}\right)^3 \frac{q_3}{16\pi}\mathcal{S}_{\mathrm{oct}}. \tag{D25}$$

Here, q_3 is given by Equation (C13) and

$$\mathcal{S}_{\mathrm{oct}} = \frac{175}{16}e_K^3\sin^3 i_K \sin 3\omega_K + \frac{15}{16}(4e_K + 3e_K^3)\sin\omega_K(4\sin i_K - 5\sin^3 i_K). \tag{D26}$$

To conclude this section, we tabulate the eigenvectors of L_x and L_y that are used in the calculations above. The eigenvectors of $L_y^{(2)}$ are denoted $v_{2\mu}^{(y)}$ for $-2 \leqslant \mu \leqslant +2$. The first column of the following matrix is $v_{2,2}^{(y)}$, the second column is $v_{2,1}^{(y)}$, and so on, to the last column, which corresponds to $v_{2,-2}^{(y)}$. These eigenvectors are orthonormal and satisfy $v_{2,\mu}^{(y)\dagger} v_{2,\nu}^{(y)} = \delta_{\mu,\nu}$, and hence the eigenmatrix below is unitary. Similar remarks apply to all of the eigenmatrices below

$$\begin{bmatrix} 1/4 & 1/2 & \sqrt{3/8} & 1/2 & 1/4 \\ i/2 & i/2 & 0 & -i/2 & -i/2 \\ -\sqrt{6}/4 & 0 & 1/2 & 0 & -\sqrt{6}/4 \\ -i/2 & i/2 & 0 & -i/2 & i/2 \\ 1/4 & -1/2 & \sqrt{3/8} & -1/2 & 1/4 \end{bmatrix}. \tag{D27}$$

The eigenvectors of $L_x^{(2)}$ are

$$\begin{bmatrix} 1/4 & -i/2 & -\sqrt{3/8} & i/2 & 1/4 \\ 1/2 & -i/2 & 0 & -i/2 & -1/2 \\ \sqrt{6}/4 & 0 & 1/2 & 0 & \sqrt{6}/4 \\ 1/2 & i/2 & 0 & i/2 & -1/2 \\ 1/4 & i/2 & -\sqrt{3/8} & -i/2 & 1/4 \end{bmatrix}. \tag{D28}$$

For calculation of the octupole, we need the eigenvectors of $L_y^{(3)}$ tabulated below

$$\frac{1}{8}\begin{bmatrix} i & \sqrt{6} & -i\sqrt{15} & -\sqrt{20} & i\sqrt{15} & \sqrt{6} & -i \\ -\sqrt{6} & 4i & \sqrt{10} & 0 & \sqrt{10} & -4i & -\sqrt{6} \\ -i\sqrt{15} & -\sqrt{10} & -i & -\sqrt{12} & i & -\sqrt{10} & i\sqrt{15} \\ \sqrt{20} & 0 & \sqrt{12} & 0 & \sqrt{12} & 0 & \sqrt{20} \\ i\sqrt{15} & -\sqrt{10} & i & -\sqrt{12} & -i & -\sqrt{10} & -i\sqrt{15} \\ -\sqrt{6} & -4i & \sqrt{10} & 0 & \sqrt{10} & 4i & -\sqrt{6} \\ -i & \sqrt{6} & i\sqrt{15} & -\sqrt{20} & -i\sqrt{15} & \sqrt{6} & i \end{bmatrix}. \tag{D29}$$

Finally, the eigenvectors of $L_x^{(3)}$ are as follows:

$$\frac{1}{8}\begin{bmatrix} 1 & -i\sqrt{6} & -\sqrt{15} & i\sqrt{20} & \sqrt{15} & -i\sqrt{6} & -1 \\ \sqrt{6} & -4i & -\sqrt{10} & 0 & -\sqrt{10} & 4i & \sqrt{6} \\ \sqrt{15} & -i\sqrt{10} & 1 & -i\sqrt{12} & -1 & -i\sqrt{10} & -\sqrt{15} \\ \sqrt{20} & 0 & \sqrt{12} & 0 & \sqrt{12} & 0 & \sqrt{20} \\ \sqrt{15} & i\sqrt{10} & 1 & i\sqrt{12} & -1 & i\sqrt{10} & -\sqrt{15} \\ \sqrt{6} & 4i & -\sqrt{10} & 0 & -\sqrt{10} & -4i & \sqrt{6} \\ 1 & i\sqrt{6} & -\sqrt{15} & -i\sqrt{20} & \sqrt{15} & i\sqrt{6} & -1 \end{bmatrix}. \tag{D30}$$

Appendix E
Dynamics

We now analyze the effect of MOND on the dynamics of a KBO. In Lagrangian or Hamiltonian mechanics, the state of the KBO would be specified by its position and velocity or by its position and canonical momentum—a total of six dynamical variables or three degrees of freedom. In celestial mechanics, it is more convenient to work with a noncanonical set of variables, the orbital elements (a_K, e_K, ω_K, i_K, Ω_K, and f_K). a_K and e_K specify the shape of the instantaneous orbit (the orbit that the KBO would pursue if all influences except the Newtonian gravity of the Sun were turned off); ω_K, i_K, and Ω_K specify the orientation of the orbit; and f_K specifies the location of the KBO along the orbit. To be precise, f_K is the angle between the position vector of the KBO and the apsidal vector joining the Sun to the perihelion. The dynamics of the orbital elements is determined by the disturbing function via Lagrange's equations.

In the secular approximation, we focus on the behavior of the orbital elements on timescales that are long compared to the orbital period of the instantaneous orbit. In this approximation, the disturbing function is time averaged over the orbit, and the anomaly f_K is eliminated from the equations. Furthermore, it turns out that in the secular approximation the semimajor axis a_K is conserved and may be regarded as a fixed parameter (Murray & Dermott 2000). Hence, in the secular approximation there are only four dynamical variables (e_K, ω_K, i_K, and Ω_K) and two degrees of freedom. The dynamics of these variables are governed by the following Lagrange equations:

$$\begin{aligned} m_K\frac{de_K}{dt} &= -\frac{1}{n_K a_K^2}\sqrt{1-e_K^2}\,\frac{\partial \mathcal{R}}{\partial \omega_K} \\ m_K\frac{d\Omega_K}{dt} &= \frac{1}{n_K a_K^2}\frac{1}{\sqrt{1-e_K^2}}\frac{1}{\sin i_K}\frac{\partial \mathcal{R}}{\partial i_K} \\ m_K\frac{d\omega_K}{dt} &= \frac{1}{n_K a_K^2}\frac{\sqrt{1-e_K^2}}{e_K}\frac{\partial \mathcal{R}}{\partial e_K} - \frac{1}{n_K a_K^2}\frac{\cot i_K}{\sqrt{1-e_K^2}}\frac{\partial \mathcal{R}}{\partial i_K} \\ m_K\frac{di_K}{dt} &= \frac{1}{n_K a_K^2}\frac{1}{\sqrt{1-e_K^2}}\left(\cot i_K\frac{\partial R}{\partial \omega_k} - \frac{1}{\sin i_K}\frac{\partial \mathcal{R}}{\partial \Omega_K}\right). \end{aligned} \tag{E1}$$

Here $n_K = (GM_\odot/a_K^3)^{1/2}$ is the mean angular frequency of a Kepler orbit of semimajor axis a_K.

This is a formidable set of coupled nonlinear differential equations, but for our problem, a great simplification occurs due to symmetry, allowing for an exact solution. First, it is easy to verify that the disturbing function $\mathcal{R}$ itself is a conserved quantity, by observing that

$$\frac{d\mathcal{R}}{dt} = \frac{\partial \mathcal{R}}{\partial e_K}\frac{de_K}{dt} + \frac{\partial \mathcal{R}}{\partial \Omega_K}\frac{d\Omega_K}{dt} + \frac{\partial \mathcal{R}}{\partial \omega_K}\frac{d\omega_K}{dt} + \frac{\partial \mathcal{R}}{\partial i_K}\frac{di_K}{dt}, \tag{E2}$$

and making use of Lagrange's Equations (E1). Second, due to cylindrical symmetry about the axis joining the Sun to the center of the Galaxy, $\mathcal{R}$ is independent of Ω_K. More crucially, the symmetry implies that the axial component of the angular momentum is conserved. For a Keplerian orbit, the magnitude of the angular momentum is given by $[GM_\odot m_K^2 a_K(1-e_K^2)]^{1/2}$ in terms of the orbital elements. The component along the symmetry axis is $[GM_\odot m_K^2 a_K(1-e_K^2)]^{1/2}\cos i_K$. Discarding unimportant constants, it follows that the quantity

$$h = \sqrt{1-e_K^2}\cos i_K \tag{E3}$$

is conserved. It is easy to verify explicitly by use of Lagrange's Equations (E1) that h is conserved if $\mathcal{R}$ is independent of Ω_K. We will call h the dimensionless axial angular momentum in the following discussion.

Hence, our problem is integrable. There are four dynamical variables, (e_K, ω_K, i_K, and Ω_K) and hence two degrees of freedom. There are also two conserved quantities: $\mathcal{R}$ and h.

It is useful to make the following observations based on the definition of h. (i) Since $0 \leqslant e_K \leqslant 1$ and $0 \leqslant i_K \leqslant \pi$, it follows that $|h| \leqslant 1$ with negative values of h corresponds to $\pi/2 < i_K \leqslant \pi$. (ii) For a given h, the eccentricity lies in the range $0 \leqslant e_K \leqslant \sqrt{1-h^2}$. (iii) For $h > 0$, the inclination lies in the range $0 \leqslant i_K \leqslant i_{\max}$; for $h < 0$, in the range $\pi - i_{\max} \leqslant i_K \leqslant \pi$. Here, $i_{\max} = \cos^{-1}|h|$, and it lies in the range $0 \leqslant i_{\max} \leqslant \pi/2$. (iv) Obviously if $h = 0$, then either $e_K = 1$ or $i_K = \pi/2$. (v) If $h = \pm 1$, then $e_K = 0$ and $i_K = 0$ or π, respectively.

To gain some qualitative insight into the KBO dynamics, we now work in the quadrupole approximation to the disturbing function given in Equations (D20) and (D21). We use Equation (E3) to eliminate i_K to obtain $\mathcal{S}_Q$ as a function of

(e_K, ω_K). The result is

$$\mathcal{S}_Q^{\rm eff} = -2 - 9h^2 + 15h^2\cos 2\omega_K + (15\cos 2\omega_K - 3)e_K^2 + 15h^2(1 - \cos 2\omega_K)\frac{1}{1 - e_K^2}. \quad \text{(E4)}$$

Here, $0 \leqslant e_K \leqslant \sqrt{1 - h^2}$ and $0 \leqslant \omega_K < 2\pi$. The conservation of $\mathcal{R}_Q$ implies that the KBO trajectories will lie along contours of fixed $\mathcal{S}_Q^{\rm eff}$ in the (e_K, ω_K) plane. Hence, we can visualize the dynamics by plotting the contours of fixed $\mathcal{S}_Q^{\rm eff}$.

It is easy to see that for fixed e_K, the scaled disturbing function $\mathcal{S}_Q^{\rm eff}$ oscillates as a function of ω_K with minima at $\omega_K = \pi/2$ and $3\pi/2$ and maxima at 0 and π. This is facilitated by rewriting $\mathcal{S}_Q^{\rm eff}$ in the form

$$\mathcal{S}_Q^{\rm eff} = -2 - 9h^2 - 3e_K^2 + \frac{15h^2}{1 - e_K^2} + 15\left(h^2 + e_K^2 - \frac{h^2}{1 - e_K^2}\right)\cos 2\omega_K \quad \text{(E5)}$$

and demonstrating that the coefficient of $\cos 2\omega_K$ is positive for the entire range $0 < e_K^2 < 1 - h^2$. It is also easy to see that $\mathcal{S}_Q^{\rm eff} = -2 + 6h^2$ for $e_K = 0$ and $\mathcal{S}_Q^{\rm eff} = 10 - 6h^2$ for $e_K^2 = 1 - h^2$. Remarkably, we see that $\mathcal{S}_Q^{\rm eff}$ is independent of ω_K for the extremal values of e_K. We also observe that

$$\mathcal{S}_Q^{\rm ef}(e_K^2 \to 1 - h^2) - \mathcal{S}_Q^{\rm eff}(e_K^2 \to 0) = 12(1 - h^2) \geqslant 0. \quad \text{(E6)}$$

Next let us consider the behavior of $\mathcal{S}_Q^{\rm eff}$ as a function of e_K^2 for fixed ω_K. For this purpose, it is better to revert to the form in Equation (E4). We observe that the last term in $\mathcal{S}_Q^{\rm eff}$ with the factor $1/(1 - e_K^2)$ is monotonically increasing with e_K^2 since its coefficient is positive. For the e_K^2 term, we can distinguish two cases. For $\cos 2\omega_K > 1/5$, it is monotonically increasing with e_K^2 since its coefficient is positive. For $\cos 2\omega_K \leqslant 1/5$, it is not monotonically increasing. Hence, we can definitely state that $\mathcal{S}_Q^{\rm eff}$ is monotonically increasing as a function of e_K^2 for all ω_K such that $\cos 2\omega_K > 1/5$. But for $\cos\omega_K \leqslant 1/5$, further analysis is needed. These values of ω_K correspond to two equal intervals centered on $\omega_K = \pi/2$ and $\omega_K = 3\pi/2$ with a width greater than $\pi/2$ but less than π. In these intervals, we will see that there are two possible behaviors as a function of e_K^2. Either $\mathcal{S}_Q^{\rm eff}$ can remain monotonically increasing, or it can first decrease to a minimum and then increase again as e_K^2 varies from 0 to $1 - h^2$. To determine the actual behavior that is obtained, we compute $\partial\mathcal{S}_Q^{\rm eff}/\partial e_K^2$ and find it is equal to zero for $e_K^2 \to \bar{e}^2$ where

$$\bar{e}^2 = 1 - |h|\sqrt{\frac{1 - \cos 2\omega_K}{(1/5) - \cos 2\omega_K}}. \quad \text{(E7)}$$

Obviously, we need $\cos 2\omega_K < 1/5$ for $\bar{e}^2$ to be real, but in fact we need to impose the more stringent conditions that $0 \leqslant \bar{e}^2 \leqslant 1 - h^2$. The condition that $\bar{e}^2 \leqslant 1 - h^2$ is automatically fulfilled for $(1/5) - \cos 2\omega_K > 0$ as we have assumed. But the condition that $\bar{e}^2 \geqslant 0$ translates to

$$\cos 2\omega_K \leqslant 1 - \frac{4}{5}\frac{1}{1 - h^2}. \quad \text{(E8)}$$

It is easy to see that the right-hand side of Equation (E8) decreases monotonically from $1/5$ to -1 as h^2 goes from 0 to $3/5$ and is less than -1 for $h^2 > 3/5$.

In summary, we find the following behavior for $\mathcal{S}_Q^{\rm eff}$ considered as a function of e_K^2 for fixed ω_K. (i) For $3/5 < h^2 \leqslant 1$, we find $\mathcal{S}_Q^{\rm eff}$ is monotonic increasing for all ω_K. (ii) For $0 \leqslant h^2 \leqslant 3/5$, we find that provided Equation (E8) is satisfied, $\mathcal{S}_Q^{\rm eff}$ shows nonmonotonic behavior: it decreases for $0 \leqslant e_K^2 < \bar{e}^2$ and increases for $\bar{e}^2 < e_K^2 \leqslant 1 - h^2$ with a minimum at $e_K^2 = \bar{e}^2$ where $\bar{e}^2$ is given by Equation (E7). The range of ω_K defined by Equation (E8) corresponds to two intervals centered about $\omega_K = \pi/2$ and $\omega = 3\pi/2$. Outside of this range of ω_K values, $\mathcal{S}_Q$ remains monotonic even for $0 \leqslant h^2 \leqslant 3/5$. Crucially then, we find that $\mathcal{S}_Q^{\rm eff}$ has two global minima at (e_K, ω_K) given by $(e_C, \pi/2)$ and $(e_C, 3\pi/2)$ where

$$e_C^2 = 1 - |h|\sqrt{\frac{5}{3}}. \quad \text{(E9)}$$

Equation (E9) is obtained from Equation (E7) by setting $\omega_K \to \pi/2$ or $3\pi/2$. This result for the location of the minimum is one of the key results of this section.

We are now ready to plot contours of fixed $\mathcal{S}_Q^{\rm eff}$. It is convenient to define $\Delta\mathcal{S}_Q^{\rm eff} = \mathcal{S}_Q^{\rm eff} - \mathcal{S}_Q^{\rm eff}(e_K^2 \to 0)$. Making use of Equation (D21), we find explicitly that

$$\Delta\mathcal{S}_Q^{\rm eff} = -15(1 - \cos 2\omega_K) + (15\cos 2\omega_K - 3)e_K^2 + \frac{15h^2}{(1 - e_K^2)}(1 - \cos 2\omega_K). \quad \text{(E10)}$$

Evidently $\Delta\mathcal{S}_Q^{\rm eff} = 0$ for $e_K^2 = 0$ and $\Delta\mathcal{S}_Q^{\rm eff} = 12(1 - h^2)$ for $e_K^2 = 1 - h^2$. (i) For $h^2 > 3/5$, $\Delta\mathcal{S}_Q^{\rm eff}$ increases monotonically with e_K^2 for fixed ω_K and oscillates with ω_K for fixed e_K as discussed above. Hence, we expect the contours of fixed $\Delta\mathcal{S}_Q^{\rm eff}$ to be wavy lines with maxima at $\omega_K = \pi/2$ and $3\pi/2$ and minima at $\omega_K = 0$, π and 2π. The contours for different values of $\Delta\mathcal{S}_Q^{\rm eff}$ between zero and the maximal value of $12(1 - h^2)$ may be plotted exactly by solving Equation (E10) for e_K^2 as a function of ω_K. This is a quadratic equation, and hence we have to choose the root by either verifying the pattern of maxima and minima noted above or by continuity with the expected result as $e_K^2 \to 0$. (ii) For $0 \leqslant h^2 \leqslant 3/5$, it is convenient to first plot the contour corresponding to $\Delta\mathcal{S}_Q^{\rm eff} = 0$. Equation (E10) has the trivial solution $e_K^2 = 0$ for $\Delta\mathcal{S}_Q^{\rm eff} = 0$ and a nontrivial solution

$$e_K^2 = 1 - h^2\frac{1 - \cos 2\omega_K}{1/5 - \cos 2\omega_K}. \quad \text{(E11)}$$

We require that $0 \leqslant e_K^2 \leqslant 1 - h^2$. Imposing these conditions on the right-hand side of Equation (E11), we find as expected that the nontrivial solution exists over the range of ω_K that satisfies Equation (E8). This range corresponds to two equal intervals, one centered about $\omega_K = \pi/2$ and the other centered about $\omega_K = 3\pi/2$. Plotting the trivial and nontrivial solutions in red, we see from Figure 2(b) in the main body of the paper that they define two dome-shaped regions. $\Delta\mathcal{S}_Q^{\rm eff} > 0$ outside the dome-shaped regions and $\Delta\mathcal{S}_Q^{\rm eff} < 0$ inside the domes. In particular, the domes contain the minima of $\Delta\mathcal{S}_Q^{\rm eff}$, which are

located at $(e_K, \omega_K) \rightarrow (e_C, \pi/2 \text{ or } 3\pi/2)$ where e_C is given by Equation (E9). At the minima, it is easy to compute using Equation (E10) that

$$\Delta\mathcal{S}_Q^{\rm eff} = -30\left(\sqrt{\frac{3}{5}} - |h|\right)^2. \tag{E12}$$

Thus, the minima are deepest for $|h| \rightarrow 0$. We expect the contours to be wavy lines outside the domes and loops within. To actually plot the contours, we proceed as in case (i) for the region outside the domes, plotting the appropriate solution to Equation (E10). But inside the dome, we plot both solutions to Equation (E10) over the range of ω_K for which these solutions are real. Those plots join smoothly to form the expected loops. The results are shown in Figure 2 in the main body of the paper.

Dynamically, the phase-space flow therefore corresponds to precession along the wavy lines for $h^2 > 3/5$. For $h^2 < 3/5$, the phase space breaks up into two regions: one in which the trajectories correspond to precession (i.e., monotonic increase of ω_K), and the other in which the trajectories encircle the minima, which are fixed points of the dynamics.

For the record, we provide the specific parameters used to generate Figure 2 in the main body of the paper. In (a) we chose $h = 0.9 > \sqrt{3/5}$. The allowed range of $\Delta\mathcal{S}_Q^{\rm eff}$ is $0 \leqslant \Delta\mathcal{S}_Q^{\rm eff} \leqslant 12(1 - h^2) = 2.28$. The plotted contours correspond to $\Delta\mathcal{S}_Q^{\rm eff} = 0.4, 0.8, 1.2, 1.6$ and 2.0. In (b) we chose $h = 0.5 < \sqrt{3/5}$. Outside the domes, $0 < \Delta\mathcal{S}_Q^{\rm eff} \leqslant 12(1 - h^2) = 9$. The plotted contours correspond to $\Delta\mathcal{S}_Q^{\rm eff} = 2, 4, 6$ and 8. Inside the domes, $-2.28 \ldots \leqslant \Delta\mathcal{S}_Q^{\rm eff} < 0$. The lower limit comes from Equation (E12). The plotted contours correspond to $\Delta\mathcal{S}_Q^{\rm eff} = -0.75, -1.5$ and -2.25.

Plotting the contours of $\mathcal{S}_Q^{\rm eff}$ determines the curves traced by the KBO through the (e_K, ω_K) phase space but not the direction of the flow. To obtain the direction, we must return to Lagrange's Equations (E1). Making use of the quadrupole approximation to $\mathcal{R}_Q$ in Equation (D20) and using the conservation of h defined by Equation (E3), we find

$$\begin{aligned}
\frac{de_K^2}{dt} &= \frac{60}{T_K} e_K^2 \sqrt{1 - e_K^2} \sin 2\omega_K \left[1 - \frac{h^2}{1 - e_K^2}\right], \\
\frac{d\omega_K}{dt} &= \frac{1}{T_K} \frac{1}{\sqrt{1 - e_K^2}} [-6(1 - e_K^2) + 30(1 - e_K^2)\cos 2\omega_K] \\
&\quad + \frac{1}{T_K} \frac{1}{\sqrt{1 - e_K^2}} \left[30(1 - \cos 2\omega_K) \frac{h^2}{1 - e_K^2}\right].
\end{aligned} \tag{E13}$$

Here, T_K is defined via

$$\frac{1}{T_K} = n\left(\frac{a_K}{R_M}\right)^3 \frac{q_2}{32\pi} \tag{E14}$$

and is the natural timescale for MOND induced evolution of the KBO orbit. The first of these equations is sufficient to determine the direction of the flow. We see that $de_K^2/dt \geqslant 0$ for $0 \leqslant \omega_K \leqslant \pi/2$ and $\pi \leqslant \omega_K \leqslant 3\pi/2$; and $de_K^2/dt < 0$ for $\pi/2 < \omega_K < \pi$ and $3\pi/2 < \omega_K < 2\pi$. From this, we infer that the precession is from left to right in the figure (ω_K increases monotonically with time) while the oscillations are clockwise in the figure.

It is easy to verify that if we set (e_K, ω_K) to the fixed-point values $(e_C, \pi/2 \text{ or } 3\pi/2)$ on the right-hand side of Equation (E13) then $de_K^2/dt = 0$ and $d\omega_K/dt = 0$, as expected. Linearizing the equation of motion (E13) about the fixed point yields

$$\begin{aligned}
\frac{d}{dt}\Delta e_K^2 &= \left(\frac{5}{3}\right)^{\frac{1}{4}} \frac{120|h|^{1/2}}{T_K} \left(\sqrt{\frac{3}{5}} - |h|\right)\left(\sqrt{\frac{5}{3}} - |h|\right)\Delta\omega_K \\
\frac{d}{dt}\Delta\omega_K &= -\left(\frac{3}{5}\right)^{\frac{1}{4}} \frac{72}{T_K|h|^{1/2}} \Delta e_K^2
\end{aligned} \tag{E15}$$

where $\Delta e_K^2 = e_C^2 - e_K^2$ and $\Delta\omega_K = \omega_K - \pi/2$ or $\Delta\omega_K = \omega_K - 3\pi/2$. From Equation (E15), we see that the frequency of small oscillations about the fixed point is

$$\frac{\sqrt{8640}}{T_K}\left(\sqrt{\frac{3}{5}} - |h|\right)^{1/2}\left(\sqrt{\frac{5}{3}} - |h|\right)^{1/2}. \tag{E16}$$

We see that the frequency increases monotonically as $|h| \rightarrow 0$, reaching the maximum value of

$$\frac{24\sqrt{15}}{T_K}. \tag{E17}$$

Thus far we have focused on the dynamics of e_K and ω_K. The dynamics of i_K are latched to those of e_K by the conservation of h via Equation (E3). It is worth noting explicitly that at the fixed point $(e_C, \pi/2 \text{ or } 3\pi/2)$ that

$$\cos i_K = \left(\frac{3}{5}\right)^{1/4} \text{sgn}(h)\ |h|^{1/2}. \tag{E18}$$

This is established using Equations (E9) and (E3). Here, $\text{sgn}(h) = +1$ for $h > 0$ and $\text{sgn}(h) = -1$ for $h < 0$. It follows that $e_C \rightarrow 1$ as $h \rightarrow 0$ and $i_K \rightarrow \pi/2$. More precisely,

$$i_K \approx \frac{\pi}{2} - \left(\frac{3}{5}\right)^{1/4} \text{sgn}(h)\ |h|^{1/2} \tag{E19}$$

for small h.

The dynamics of Ω_K is also fully determined by that of e_K and ω_K. To see this, we return to the Lagrange Equations (E1) and make use of the quadrupole approximations in Equations (D20) and (D21) and of the conservation law in Equation (E3) to obtain

$$\frac{d\Omega_K}{dt} = -\frac{1}{T_K} \frac{h}{(1 - e_K^2)} [12(1 - e_K^2) + 30e_K^2(1 - \cos 2\omega_K)]. \tag{E20}$$

We see that if e_K and ω_K are known functions of time, we can readily integrate Equation (E20) to obtain Ω_K. It is also evident from Equation (E20) that $d\Omega_K/dt < 0$ for $h > 0$ and $d\Omega_K/dt > 0$ for $h < 0$. In either case, Ω_K varies monotonically in time although it may not do so uniformly. To obtain the behavior of Ω_K when (e_K, ω_K) are at a fixed point, we set $e_K \rightarrow e_C$ and

$\omega_K \to \pi/2$ or $3\pi/2$ in Equation (E20). We obtain

$$\frac{d\Omega_K}{dt} = -\frac{1}{T_K}\,\mathrm{sgn}(h)\,\sqrt{\frac{3}{5}}\left[60 - 48\sqrt{\frac{5}{3}}\,|h|\right]. \tag{E21}$$

In other words, we obtain uniform precession in Ω_K at the fixed point with $d\Omega_K/dt = 0$ for the special case that $h = 0$.

Thus far, we have worked with the quadrupole approximation to the disturbing function. We now consider how the integrable dynamics above is modified by the octupole correction given by Equations (D25) and (D26). In particular, we are interested in how the two fixed points located at (e_C, $\pi/2$) and (e_C, $3\pi/2$) are affected. We find that the octupole term shifts the locations of these fixed points slightly, but more crucially it makes the fixed point at (e_C, $\pi/2$) less stable than the one at (e_C, $3\pi/2$). Hence, it is the latter fixed point that will be dominant in shaping the anomalous structure of the Kuiper Belt.

We sketch briefly how these results are established. The octupole term respects the cylindrical symmetry of the problem, so h remains conserved, and we can use Equation (E3) to eliminate i_K from Equation (D26). Setting (e_K, ω_K) to the two fixed-point values, we see that $\mathcal{R}_{\rm oct}^{\rm eff}$ is positive at the first fixed point and negative at the second consistent with the idea that the octupole term is destabilizing the first and stabilizing the second. In order to make this quantitative, we expand $\mathcal{R}_{\rm oct}^{\rm eff}$ around each of the fixed points to quadratic order. For the fixed point located at (e_C, $\pi/2$) in the quadrupole approximation, we find that it shifts to a slightly higher value of e_K and becomes less stable, as evidenced by the frequency of small oscillations about the fixed point, which becomes lower. For the fixed point at (e_C, $3\pi/2$) in the quadrupole approximation, we find that it shifts to a slightly lower value of e_K and becomes more stable as evidenced by the frequency of small oscillations, which becomes higher. The formulae for the shifts in position and frequencies are long and not very illuminating, so for brevity we omit them.

Now let us consider the effect of symmetry breaking perturbations on the integrable MOND induced dynamics considered so far. The perturbations include nonsecular terms in the MOND disturbing function as well as secular and nonsecular perturbations caused by the giant planets. For the long time dynamics, the slow variation in the symmetry axis as the Sun rotates around the galaxy must also be considered (for an analogous problem, see Banik & Zhao 2018b). According to Hamiltonian chaos theory (Percival & Richards 1983), the phase-space flow will become chaotic under these perturbations, but the regular flow around the stable fixed point (e_C, $3\pi/2$) should persist especially for small h. Hence, we predict that a population of KBOs should be found in orbits close to the stable fixed point for small h (we will specify below the relevant values of h). This is the central result of the paper.

Let us describe more fully the key characteristics of the orbits of this predicted KBO population that are stabilized by the galactic field in MOND. Recall that we are using as the reference plane not the mean ecliptic but rather the plane perpendicular to the direction to the center of the Galaxy. Thus, an orbit with $\omega_K = 3\pi/2$ and $i_K = \pi/2$ will have its apsidal vector $\hat{\boldsymbol{\alpha}}_K$ pointing directly away from the center of the galaxy. Here, $\hat{\boldsymbol{\alpha}}_K$ is a unit vector that points from the Sun to the perihelion. This would be the case for a fixed-point orbit with $h = 0$. However, as we will explain momentarily, we expect h to be small for reasons of stability, but greater than a minimum threshold value $h_{\rm min}$ that depends on the seminar major axis a_K. Thus, we expect the orbits to have $i_K \approx \pi/2$ and for the apsidal vector $\hat{\boldsymbol{\alpha}}_K$ to be inclined at a small angle $(\pi/2 - i_K)$ relative to $-\hat{\boldsymbol{n}}_G$. Here, $\hat{\boldsymbol{n}}_G$ is the unit vector that points from the Sun to the center of the galaxy.

Let us denote by A_K the angle between $\hat{\boldsymbol{\alpha}}_K$ and $\hat{\boldsymbol{n}}_G$. We can estimate the expected range of A_K as follows. For a given h in the range $0 \leqslant h^2 \leqslant 3/5$, the orbital elements ($e_K$, ω_K) of the stable fixed point are (e_C, $3\pi/2$) in the quadrupole approximation. Here, e_C is given by Equation (E9). Making use of Equations (E3) and (E9), we conclude that

$$\cos i_K = \left(\frac{3}{5}\right)^{1/4} \mathrm{sgn}\,(h)\,|h|^{1/2} \tag{E22}$$

at the fixed point. Now, $A_K = \pi/2 + i_K$, which leads to

$$\hat{\boldsymbol{\alpha}}_K \cdot \hat{\boldsymbol{n}}_G = \cos A_K = -\sqrt{1 - \left(\frac{3}{5}\right)^{1/2} |h|}\,. \tag{E23}$$

Assuming that $0 < |h| \leqslant (3/5)^{1/2}$, it follows that $129^\circ < A_K \leqslant 180^\circ$. Taking into account that the lower bound on $|h|$ is $h_{\rm min}$, we can refine our estimate to read

$$129^\circ < A_K < \cos^{-1}\left(-\sqrt{1 - \left(\frac{3}{5}\right)^{1/2} h_{\rm min}}\right). \tag{E24}$$

We will see below that for $a_K \gg a_8$, $h_{\rm min} \to 0$ and the upper limit of the range of expected A_K approaches 180°. By contrast, in the absence of MOND, the Galactic field has no significant effect on KBOs, and there should be no correlation between $\hat{\boldsymbol{\alpha}}_K$ and $\hat{\boldsymbol{n}}_G$.

Next, let us explain the origin of the bound $h_{\rm min}$. The closest approach of the KBO to the Sun is $a_K(1 - e_K)$. For the orbit to be detached from the inner solar system, we need

$$a_K(1 - e_K) > a_8. \tag{E25}$$

Taking e_K to be the fixed-point value e_C given by Equation (E9), we find that Equation (E25) leads to the condition that $|h| > h_{\rm min}$ where

$$h_{\rm min} = \sqrt{\frac{3}{5}}\left[1 - \left(1 - \frac{a_8}{a_K}\right)^2\right]. \tag{E26}$$

For $a_K \gg a_8$, we see that $h_{\rm min} \sim 2\sqrt{3/5}\,a_8/a_K \to 0$ as $a_K \to \infty$ as noted above.

Finally, let us comment briefly on the orbit normal $\hat{\boldsymbol{l}}_K$. Obviously $\hat{\boldsymbol{l}}_K$ must be perpendicular to $\hat{\boldsymbol{\alpha}}_K$, and hence we expect $\hat{\boldsymbol{l}}_K$ to be roughly at 90° to $\hat{\boldsymbol{n}}_G$ as well to the same extent that $\hat{\boldsymbol{\alpha}}_K$ is antialigned with $\hat{\boldsymbol{n}}_G$. However, due to precession of Ω_K, we expect $\hat{\boldsymbol{l}}_K$ to be as random as possible, consistent with the constraint that it is strictly perpendicular to $\hat{\boldsymbol{\alpha}}_K$. Since $\hat{\boldsymbol{n}}_G$ lies almost in the ecliptic plane, it follows that the predicted population of KBOs may be found in the ecliptic plane as well as at high inclinations to it.

In summary, the main result of this section is the prediction that there is a population of KBOs with orbits clustered in the (e_K, ω_K) phase space near the stable fixed point of the dynamics. The fixed point is at (e_C, $3\pi/2$) in the quadrupole approximation where e_C is given by Equation (E9). We have described the orbital characteristics of this population, and in the next section we will show that an observed population of

KBOs does indeed have orbits consistent with the predicted characteristics.

Appendix F
Comparison to Data

There are several well-established families of KBOs. Many KBOs are in orbits that are locked in 2:1 or 3:2 resonances with Neptune. The classical KBOs have semimajor axes that lie between the two resonances noted above. Centaurs penetrate the inner solar system but also recede far beyond the orbit of Neptune. The scattered disk consists of KBOs that recede far beyond the orbit of Neptune but have a perihelion distance comparable to that of Neptune. Recently, a new subclass of this family has been recognized: objects that have perihelion distances well beyond the semimajor axis of Neptune and highly eccentric orbits that carry them to the outer reaches of the solar system. Sedna (Brown et al. 2004) and 2012 VP_{113} (Trujillo & Sheppard 2014) were the first members of this subclass to be discovered. We will therefore call this the Sedna family of KBOs.

The orbits of KBOs are for the most part compatible with dynamical models of the solar system based on eight planets and Newtonian gravity. The Sedna family are a notable exception. The Planet Nine hypothesis was introduced to explain the anomalous structure of their orbits. Here, we will explore the alternative hypothesis that this anomalous structure is due to the Galactic field in MOND. Because their orbits are detached from the inner solar system, the Sedna family are a particularly clean and sensitive probe of MOND effects and are the exclusive focus of this paper. However, we note that the Centaurs also pose a puzzle: they have a broad distribution of inclinations with many cases of very high inclination and even retrograde motion. The dynamics of Centaurs are chaotic and complicated by their penetration into the inner solar system and therefore not considered further here. However, the finding in the previous section that MOND effects can lead to orbits with very high inclinations is potentially significant in this context and may be worth further consideration.

In their comprehensive review of the Planet Nine hypothesis, Batygin et al. (2019) identified six members of the Sedna family that dynamical simulations reveal have stable orbits under the influence of the known planets and eight more that have metastable orbits. These 14 objects were the trans-Neptunian objects in the Minor Planet Database of the International Astronomical Union whose orbital parameters satisfied the criteria that $a \geqslant 250$ au, $q \geqslant 30$ au (where q denotes the perihelion distance) and $i \leqslant 40^\circ$ as of 2018 October 10. As of 2022 June 21, there are eight additional objects that meet these criteria in the International Astronomical Union database. Table 1 lists the orbital parameters for all 22 KBOs: the 14 discussed in the review by Batygin et al. (2019) as well as the eight additional ones that are now known. These data are taken from the Minor Planet Database; references to the discovery papers and the primary observational literature may be found on the website of the minor planet center. Note that for all 22 KBOs, $q > a_8$ where $a_8 = 30.07$ au is the semimajor axis of Neptunes nearly circular orbit. These KBOs are a good testing ground for the Planet Nine hypothesis and also for MOND effects. In the main body of the paper, we limited ourselves to the six with stable orbits, as they are likely the most clear-cut members of the new population of KBOs that we predict based on MOND. Here also our main focus is on the same six KBOs, but in addition we show that the orbits of the eight metastable objects and the eight new ones are also compatible with MOND.

Table 1
Orbital Elements of KBOs of the Sedna Family

Object	ω	Ω	i	e	q (au)	a (au)
Sedna	311.°1	144.°2	11.°9	0.85	76.37	510.39
TG387[a]	118.°0	300.°8	11.°7	0.94	65.04	1031.49
2012 VP_{113}	293.°5	90.°7	24.°1	0.69	80.39	258.27
VN112[b]	326.°8	66.°0	25.°6	0.85	47.30	318.97
GB174	347.°0	130.°9	21.°6	0.86	48.61	336.67
SR349	340.°0	34.°8	18.°0	0.84	47.69	302.23
RX245	64.°6	8.°6	12.°1	0.90	45.73	448.49
KG163	32.°3	219.°1	14°	0.95	40.49	776.24
GT50	129.°3	46.°1	8.°8	0.88	38.48	324.66
TG422	285.°6	112.°9	18.°6	0.92	35.55	468.98
FE72	133.°5	337°	20.°7	0.98	36	1586.3
SY99	31.°7	29.°5	4.°2	0.94	50.1	815.97
RF98	311.°6	67.°6	29.°6	0.90	36.07	357.63
FT28	40.°8	217.°7	17.°4	0.85	43.41	297.64
EU5	109.°5	109.°3	18.°3	0.95	46.65	973.47
VM35	303.°6	192.°3	8.°5	0.84	44.61	283.12
SD106	162.°6	219.°4	4.°8	0.89	42.75	378.97
WB556	235.°5	114.°8	24.°2	0.86	42.7	299.72
TU115	225.°1	192.°3	23.°5	0.90	35.01	344.29
SL102	265.°5	94.°7	6.°5	0.89	38.12	338.01
RA109	262.°9	104.°7	12.°4	0.91	45.99	504.02
FL28	225°	294.°5	15.°8	0.90	32.17	336.45

Notes. The data are from the Minor Planet Database of the International Astronomical Union. As discussed in the review by Batygin et al. (2019), the first six have stable orbits under the influence of the known planets; the next eight are metastable. The final eight have been added to the database since the publication of the review (between 2018 October 10 and 2022 June 21).
[a] TG387 is named Leleakuhonua.
[b] VN112 is named Alicanto.

The orientation of the orbits is specified relative to the mean ecliptic plane, which is taken to be the X–Y plane. In the reference orientation, the orbit of a KBO is assumed to lie in the X–Y plane with the perihelion along the positive X-axis. The equation of the orbit in the reference configuration is therefore

$$\begin{aligned} X &= a_K \cos\xi - a_K e_K \\ Y &= a_K \sqrt{1 - e_K^2}\, \sin\xi \\ Z &= 0. \end{aligned} \tag{F1}$$

Here, $0 \leqslant \xi < 2\pi$ and a_K and e_K can be looked up from Table 1. The actual orientation of the orbit is found by rotating it about the Z-axis by ω, then about the X-axis by i, and again the Z-axis by Ω. After these transformations, the equation of the orbit is given by

$$\begin{aligned} X &= (a_K \cos\xi - a_K e_K)(\cos\omega\cos\Omega - \sin\omega\sin\Omega\cos i) \\ &\quad + a_K\sqrt{1 - e_K^2}\,\sin\xi(-\sin\omega\cos\Omega - \cos\omega\sin\Omega\cos i) \\ Y &= (a_K \cos\xi - a_K e_K)(\cos\omega\sin\Omega + \sin\omega\cos\Omega\cos i) \\ &\quad + a_K\sqrt{1 - e_K^2}\,\sin\xi(-\sin\omega\sin\Omega + \cos\omega\cos\Omega\cos i) \\ Z &= (a_K \cos\xi - a_K e_K)(\sin\omega\sin i) \\ &\quad + a_K\sqrt{1 - e_K^2}\,\sin\xi(\cos\omega\sin i). \end{aligned} \tag{F2}$$

In the ecliptic frame, the latitude and longitude are denoted (β, λ). $\hat{\boldsymbol{n}}_G$, the unit vector that points in the direction of the Galactic center, therefore has the components ($\cos\beta\cos\lambda$, $\cos\beta\sin\lambda$, $\sin\beta$) with $\beta = -5.^\circ5$ and $\lambda = 266.^\circ4$.

Using this information, we can plot the orbits of all six KBOs projected into the ecliptic plane, and we can also project the vector $\hat{\boldsymbol{n}}_G$ into the ecliptic plane. This leads to the plot shown in Figure 3 in the main body of the paper. Note that the orbits as well as $\hat{\boldsymbol{n}}_G$ lie almost in the ecliptic plane, so this visualization gives an accurate impression of their relative orientation. We see from this figure that the orbits have a remarkable alignment of their apsidal vectors. This striking alignment was discovered and highlighted by Trujillo & Sheppard (2014) and Batygin & Brown (2016a). But we see now that in addition, the orbits are well aligned with the direction to the center of the Galaxy—a feature that arises naturally in MOND but not in Newtonian gravity. Intuitively, the MOND alignment can be understood as follows. In secular perturbation theory, we think of the orbits as wires with a nonuniform density. The perihelion is the lighter end of the wire, and the aphelion is the heavy end. We see that the orbits are aligned with the heavy end toward the Galactic center, consistent with the idea that the orbits are responding to the Galactic field.

We now quantify the degree of alignment, but before that, it is worth noting here that in our dynamical analysis we used a different coordinate system. The reference plane was perpendicular to $\hat{\boldsymbol{n}}_G$, the unit vector that points in the direction of the center of the Galaxy. We took the y-axis to point in the direction of $\hat{\boldsymbol{n}}_G$ and the reference plane to be the z–x plane. In the reference configuration, the orbit lay in the z–x plane with the perihelion along the positive z-axis. The actual configuration is obtained by an R_y–R_z–R_y sequence of rotations by ω_K, i_K, and Ω_K. We distinguish the two systems notationally by using uppercase letters (X, Y, Z) for the ecliptic frame and lowercase letters (x, y, z) for the frame that we used in the dynamical analysis. For the orientation variables, we write (ω, i, Ω) without subscripts in the ecliptic frame and with subscripts (ω_K, i_K, Ω_K) in the frame used for the dynamical analysis.

In order to quantify the alignment, it is useful first to calculate the apsidal vectors $\hat{\boldsymbol{\alpha}}_K$ in the XYZ frame. We note that $\hat{\boldsymbol{\alpha}}_K$ points along the positive X-axis when the orbit is in the reference orientation. After being rotated to its actual orientation specified by (ω, i, Ω), the vector $\hat{\boldsymbol{\alpha}}_K$ is given by

$$\hat{\boldsymbol{\alpha}}_K = \begin{pmatrix} \cos\omega\cos\Omega - \sin\omega\sin\Omega\cos i \\ \cos\omega\sin\Omega + \sin\omega\cos\Omega\cos i \\ \sin\omega\sin i \end{pmatrix}. \tag{F3}$$

One way to quantify the alignment of the apsidal vectors with $\hat{\boldsymbol{n}}_G$ is to compute the mean value of $\hat{\boldsymbol{\alpha}}_K \cdot \hat{\boldsymbol{n}}_G$ for the six KBOs of interest. We obtain the value -0.68 for this alignment parameter. Note that the alignment parameter is negative, reflecting that the apsidal vectors are antialigned with $\hat{\boldsymbol{n}}_G$. In the absence of MOND, there should be no correlation between $\hat{\boldsymbol{n}}_G$ and the apsidal vectors, and the expected value of the alignment parameter is zero. If we take as the null hypothesis that the apsidal vectors should be independent unit vectors uniformly distributed over the unit sphere, then the observed value of the alignment parameter is three standard deviations away from the expected value of zero. Another way to quantify the alignment of the apsidal vectors is to note that the six values of $\hat{\boldsymbol{\alpha}}_K \cdot \hat{\boldsymbol{n}}_G$ lie in the range -1 to -0.3. The probability of that happening by chance is approximately 1 in 500. Thus, we see that the degree of alignment is highly unlikely to be due to chance. Finally in Table 2 we enumerate the values of A_K, the angle between $\hat{\boldsymbol{\alpha}}_K$ and $\hat{\boldsymbol{n}}_G$, for all six KBOs. In the preceding section, we had estimated that these angles should lie between 129° and an upper bound that depends on a_K. That upper bound is also listed in Table 2 for each KBO. Considering the crudeness of the estimated bounds, the observed values are in reasonable agreement with the predicted range.

Table 2
Alignment Angle A_K and Scaled Axial Angular Momentum h for Six KBOs of the Sedna Family Compared to Estimated MOND Upper Bound on A_K and Lower Bound on $|h|$

Object	A_K	$A_{\max}$	h	$h_{\min}$
Sedna	166°	177°	−0.14	0.003
TG387[a]	151°	179°	0.0069	0.0007
2012 VP_{113}	117°	175°	−0.085	0.01
VN112[b]	128°	176°	0.033	0.007
GB174	147°	176°	−0.18	0.006
SR349	110°	176°	0.081	0.008

Notes.
[a] TG387 is named Leleakuhonua.
[b] VN112 is named Alicanto.

We can quantify the alignment of the apsidal vectors with $\hat{\boldsymbol{n}}_G$ by asking what is the probability that the alignment parameter (the mean value of $\hat{\boldsymbol{\alpha}}_K \cdot \hat{\boldsymbol{n}}_G$) would be less than the observed value of -0.68 under the null hypothesis that the apsidal unit vectors $\boldsymbol{\alpha}_K$ are independent and uniformly distributed in orientation. A simple calculation shows that this probability is 0.0011 or approximately 1 in 1000.

We can better quantify the alignment of the apsidal vectors with $\hat{\boldsymbol{n}}_G$ by using the Kolmogorov–Smirnov test as follows. We define

$$u_i = \frac{1}{2}(1 + \hat{\boldsymbol{\alpha}}_{Ki} \cdot \hat{\boldsymbol{n}}_G) \tag{F4}$$

where $\hat{\boldsymbol{\alpha}}_{Ki}$ is the apsidal vector of the ith KBO in the data set. $i = 1, 2, \ldots, n$ where $n = 6$ if we only consider the six KBOs that are known to have stable orbits. Our prediction is that the u_i-values should cluster close to zero (since zero corresponds to perfect antialignment between $\hat{\boldsymbol{\alpha}}_{Ki}$ and $\hat{\boldsymbol{n}}_G$). By contrast, the null hypothesis is that the u_i-values are uniformly distributed random variables over the range $0 \leqslant u_i \leqslant 1$ (this follows from the hypothesis that the $\hat{\boldsymbol{\alpha}}_{Ki}$ are uniformly distributed over the unit sphere).

To qualitatively compare the data to the null hypothesis, we plot the staircase

$$C(u) = \sum_{i=1}^{n} \Theta(u - u_i) \tag{F5}$$

where Θ denotes the step function [$\Theta(x) = 1$ for $x > 0$ and $\Theta(x) = 0$ otherwise]. $C(u)$ should be compared to

$$K(u) = u, \tag{F6}$$

which is the cumulative distribution function corresponding to the null hypothesis. Figure 7 shows plots of $C(u)$ and $K(u)$ for

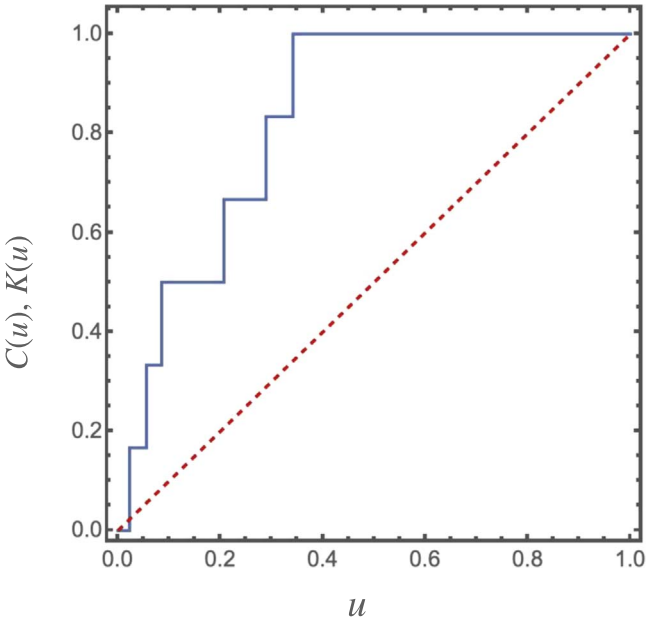

Figure 7. Plot of the $C(u)$ staircase (blue) for the six KBOs of the Sedna family that are known to have stable orbits. Also shown is $K(u)$, the cumulative distribution function for the null hypothesis (red dashed line).

the six stable KBOs; we see that the data depart markedly from the null hypothesis.

To quantitatively compare the data to the null hypothesis, we calculate the maximum vertical deviation between the null cumulative distribution function and the data staircase,

$$\Delta = \max_{0 \leqslant u \leqslant 1} |C(u) - K(u)|. \tag{F7}$$

We find the deviation for the case of the six stable objects $\Delta_6 = 0.658562\ldots$. The Kolmogorov–Smirnov statistic is the probability that a deviation greater than that observed will arise on the basis of the null hypothesis. Using the Kolmogorov–Smirnov formula (see, for example, Press et al. 1998), we find that the probability of a deviation as large as Δ_6 for $n = 6$ is 0.0054… or approximately 1 in 200.

According to Press et al. (1998), although the Kolmogorov–Smirnov formula is asymptotic for large n, it is quite accurate for n as small as 4. To confirm this, we have calculated the Kolmogorov–Smirnov statistic by a second method. We simulate a large number ($N = 300{,}000$) of sets of data based on the null hypothesis. Each data set consists of n random numbers drawn from a uniform distribution over the unit interval. For each simulated data set, we calculate Δ, and then we determine the fraction of data sets for which Δ exceeds the measured value Δ_n. This fraction is an estimate of the Kolmogorov–Smirnov statistic. Using this method, we obtain the values 0.0045… for $n = 6$. We see that the Kolmogorov–Smirnov formula overshoots slightly, but it is quite accurate even for $n = 6$. Hence, the null hypothesis is falsified at a high level of significance.

Thus, we see that the apsidal vectors of the six KBOs are aligned with the direction to the Galactic center, and this alignment is compatible with expectations based on MOND. To strengthen this conclusion, we must look to future surveys to provide a larger observational sample, and we need to refine the predictions of the MOND model by carrying out large-scale numerical simulations of KBO dynamics in MOND.

In the literature, the aspidal alignment of Sedna family KBOs is sometimes quantified by reporting the clustering of their longitudes of perihelion $\varpi = \omega + \Omega$ in the ecliptic frame. As noted in the main text, we prefer to use $\hat{\boldsymbol{\alpha}}_K \cdot \hat{\boldsymbol{n}}_G$ as a measure of alignment because it is frame invariant and unambiguously a measure of alignment. However, we have verified that the clustering predicted by our model in ω_K and i_K (together with complete randomization in Ω_K) does translate into a clustering in ϖ for orbits with $i < 40°$.

Table 2 also includes the calculated value of the scaled axial angular momentum h for each KBO along with the lower bound $h_{\rm min}$. We explain below how $\cos i_K$ can be computed from the known orbital data using Equation (F9). Using the computed values of $\cos i_K$, the tabulated values of e_K and Equation (E3), we can compute the values of h for each KBO. $h_{\rm min}$ can be computed using Equation (E26), and the tabulated values of a_K. We see that the h data lie in the range $h_{\rm min} < |h| < \sqrt{3/5}$ and generally toward the lower end of it as expected for stability in the MOND analysis.

Thus far we have focused on the six Sedna family members with stable orbits, the best exemplars of this class. Figure 8 shows the orbits of all 14 KBOs discussed in the review by Batygin et al. (2019). Figure 9 shows the orbits of all 22 KBOs in Table 1 including the eight new ones that have been tabulated in the Minor Planet Database since the review of Batygin et al. (2019). As in Figure 3, the orbits and the direction to the Galactic center are projected into the ecliptic plane. We see that the alignment between the orbits and the direction to the Galactic center persists in this larger data set. Eighteen of the 22 orbits are well aligned. We can quantify this more precisely using the Kolmogorov–Smirnov test. Figure 10 shows the staircase corresponding to all 22 objects enumerated in Table 1. The deviation of the staircase from a uniform distribution expected on the basis of the null hypothesis is quite noticeable, and we find $\Delta_{22} = 0.329609\ldots$. The corresponding Kolmogorov–Smirnoff probability is 0.0125… using the formula and 0.0123… based on our Monte Carlo evaluation described above. Thus, the null hypothesis that there is no alignment between the apsidal vectors and $\hat{\boldsymbol{n}}_G$ can be ruled out at a high level of significance. As before, the alignment of the orbits is consistent with both Planet Nine and MOND hypotheses, but the additional alignment with the Galactic center provides further support for MOND.

Finally, we can use the data in Table 1 to compute the values of ω_K and demonstrate that the six KBOs are clustered in the (e_K, ω_K) phase space, and moreover the clustering is close to the approximate location of the fixed point. To this end, it is useful to first compute the orbit normal $\hat{\boldsymbol{l}}_K$ in the XYZ frame. When the orbit is in the reference orientation, $\hat{\boldsymbol{l}}_K$ is along the positive Z-axis. After, the orbit it brought to the appropriate orientation $\hat{\boldsymbol{l}}_K$ is given by

$$\hat{\boldsymbol{l}}_K = \begin{pmatrix} \sin\Omega \sin i \\ -\cos\Omega \sin i \\ \cos i \end{pmatrix}. \tag{F8}$$

We see from Equation (F8) that $\hat{\boldsymbol{l}}_K \cdot \hat{\boldsymbol{Z}} = \cos i$. The corresponding formula for the frame used in the dynamical analysis is

$$\cos i_K = \hat{\boldsymbol{l}}_K \cdot \hat{\boldsymbol{n}}_G. \tag{F9}$$

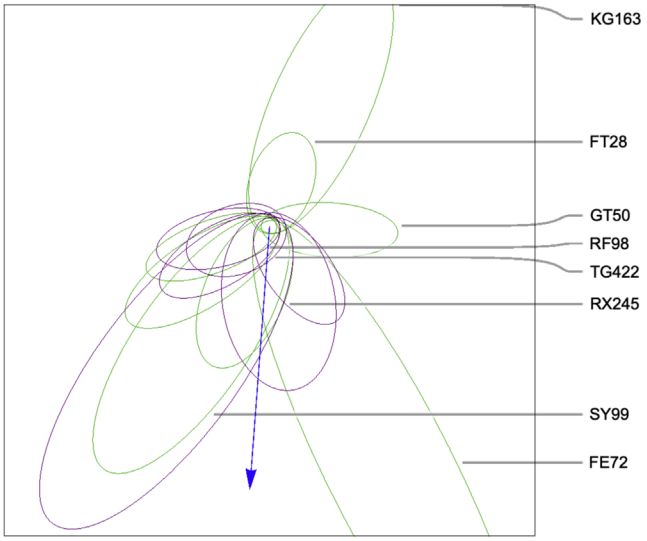

Figure 8. Orbits of 14 KBOs of the Sedna family projected onto the ecliptic plane. The blue line is parallel to the projection of $\hat{\boldsymbol{n}}_G$ onto the ecliptic plane; it points toward the center of the Galaxy. The orbits of the six KBOs that are stable are shown in purple; these are the same orbits plotted in Figure 3. Eight additional KBOs with metastable orbits are shown in green. These 14 KBOs are the ones considered in support of the Planet Nine hypothesis in the review by Batygin et al. (2019). The orbital elements are from the Minor Planet Database and are given in Table 1.

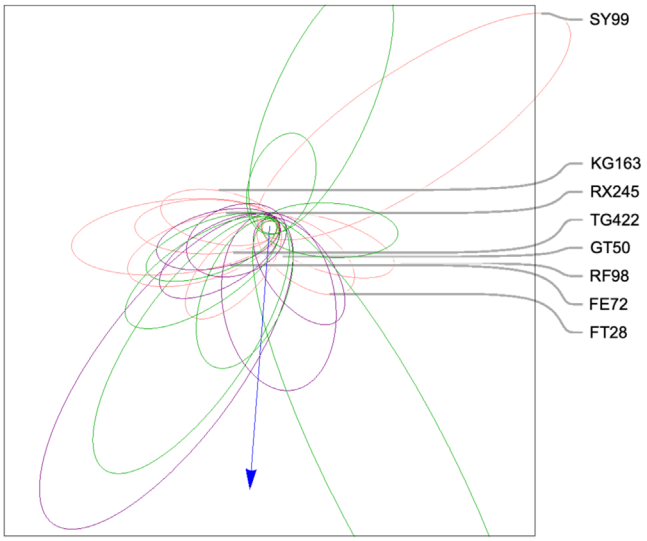

Figure 9. Same as Figure 8 with eight additional KBO orbits plotted (pink curves). These are the KBOs that have been added to the Minor Planet Database since the publication of the review by Batygin et al. (2019). The 14 objects plotted in Figure 8 are shown in purple (stable orbits) and green (metastable orbits).

Since $0 \leqslant i_K \leqslant \pi$, it follows that $\sin i_K \geqslant 0$ and $\sin i_K$ can be unambiguously calculated from $\cos i_K$. Next we observe that according to Equation (F3) $\hat{\boldsymbol{\alpha}}_K \cdot \hat{\boldsymbol{Z}} = \sin\omega \sin i$. It follows that

$$\sin\omega_K \sin i_K = \hat{\boldsymbol{\alpha}}_K \cdot \hat{\boldsymbol{n}}_G. \tag{F10}$$

By a similar argument, we can also show

$$\cos\omega_K \sin i_K = (\hat{\boldsymbol{l}}_K \times \hat{\boldsymbol{\alpha}}_K) \cdot \hat{\boldsymbol{n}}_G. \tag{F11}$$

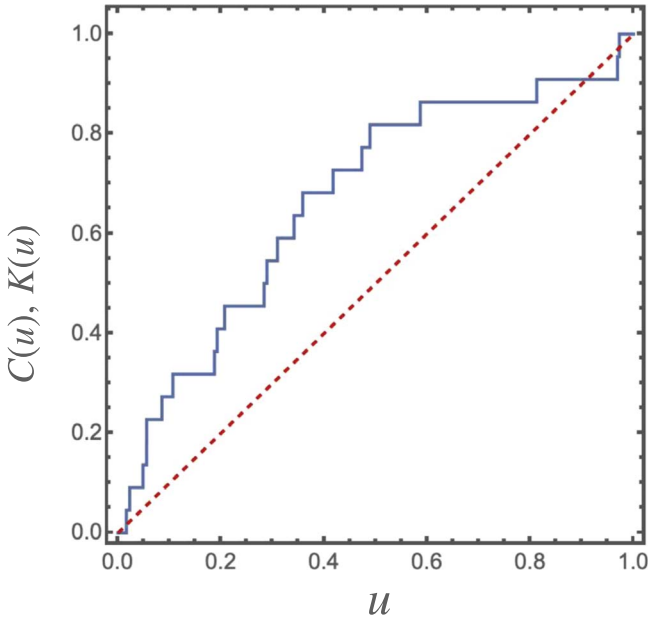

Figure 10. Plot of the $C(u)$ staircase (blue) for all 22 KBOs listed in Table 1. These objects meet the criteria used in the review article by Batygin et al. (2019) to identify potential members of the Sedna family ($a \geqslant 250$ au, $q \geqslant 30$ au and $i < 40°$). Also shown is $K(u)$, the cumulative distribution function for the null hypothesis (red dashed line).

Note that the right-hand sides of Equations (F10) and (F11) can be computed from the known forms of all three vectors in the ecliptic frame. Together, Equations (F10) and (F11) unambiguously determine ω_K. It may be worth remarking that both i_K and ω_K are fixed unambiguously once we have chosen the reference plane to be perpendicular to $\hat{\boldsymbol{n}}_G$, the direction to the center of the Galaxy. This choice is dictated by the physics and is not arbitrary. However, our choice of axes in the reference plane is arbitrary, and Ω_K will be dependent on that choice. Hence, it is not meaningful to speak of clustering in Ω_K or $\varpi_K = \omega_K + \Omega_K$, but it is meaningful to examine clustering in ω_K, as we now proceed to do.

Figure 4 shows the clustering of the six KBOs in the (e_K, ω_K) plane. The ω_K values were calculated using Equations (F9), (F10), and (F11), and the e_K values are those enumerated in Table 1. These points are shown in blue. Also shown in red in the same plot are the locations of the corresponding fixed points $(e_C, 3\pi/2)$ in the quadrupole approximation. We see that the Sedna family of KBOs is clustered close to the fixed points in phase space, as predicted. Figure 11 shows that the clustering in phase space persists when we include all 22 KBOs enumerated in Table 1: the six with stable orbits shown in the main body of the paper as well as the eight with metastable orbits and the eight that have appeared in the Minor Planet Database since the publication of the review by Batygin et al. (2019).

To strengthen the evidence for phase-space clustering, we must look to future surveys to provide a larger observational sample of KBOs of the Sedna family. Also, numerical simulations of the dynamics will allow for a more precise location of the fixed point and its domain of stability. These calculations are underway.

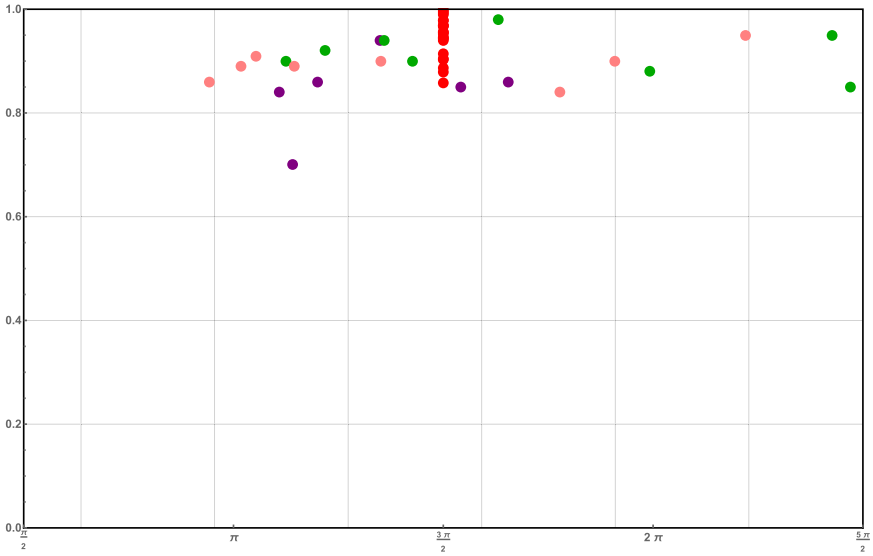

Figure 11. Plot of (e_K^2, ω_K^2) for all 22 KBOs of the Sedna family listed in Table 1 (purple points for the six KBOs known to have stable orbits, green points for those with metastable orbits, and pink points for the eight added to the Minor Planet Database since the publication of the review by Batygin et al. 2019). Also shown is the location of the corresponding fixed point of the MOND orbital dynamics in the quadrupole approximation (red points). The clustering shown in Figure 4 for the six KBOs with known stable orbits is seen to persist for all 22 KBOs.

ORCID iDs

Katherine Brown https://orcid.org/0000-0002-1567-5620
Harsh Mathur https://orcid.org/0000-0003-4451-8963

References

Abazajian, K. N., Adshead, P., Ahmed, Z., et al. 2016, arXiv:1610.02743
Asencio, E., Banik, I., & Mieske, S. 2022, MNRAS, 515, 2981
Banik, I., & Kroupa, P. 2019, MNRAS, 487, 2665
Banik, I., & Zhao, H. 2018a, MNRAS, 473, 419
Banik, I., & Zhao, H. 2018b, MNRAS, 480, 2660
Banik, I., & Zhao, H. 2022, Symm, 14, 1331
Bannister, M. T., Gladman, B. J., Kavelaars, J. J., et al. 2018, ApJS, 236, 18
Bannister, M. T., Kavelaars, J. J., Petit, J.-M., et al. 2016, AJ, 152, 70
Batygin, K., Adams, F. C., Brown, M. E., & Becker, J. C. 2019, PhR, 805, 1
Batygin, K., & Brown, M. E. 2016a, AJ, 151, 22
Batygin, K., & Brown, M. E. 2016b, ApJL, 833, 3
Begeman, K. G., Broeils, A. H., & Sanders, R. H. 1991, MNRAS, 249, 523
Bekenstein, J., & Milgrom, M. 1984, ApJ, 286, 7
Bernardinelli, P. H., Bernstein, G. M., Sako, M., et al. 2020a, ApJS, 247, 32
Bernardinelli, P. H., Bernstein, G. M., Sako, M., et al. 2020b, PSJ, 1, 28
Brada, R., & Milgrom, M. 1995, MNRAS, 276, 453
Brown, K., Abraham, R., Kell, L., & Mathur, H. 2018, NJPh, 20, 063042
Brown, M. E., & Batygin, K. 2016, ApJL, 824, 2
Brown, M. E., & Batygin, K. 2019, AJ, 157, 62
Brown, M. E., Trujillo, C. A., & Rabinowitz, D. 2004, ApJ, 617, 645
Chae, K.-H. 2022, AJ, 941, 55
Chae, K.-H., Desmond, H., Lelli, F., McGaugh, S., & Schombert, J. M. 2021, ApJ, 921, 104
Chae, K.-H., Lelli, F., & Desmond, H. 2020, ApJ, 904, 51
Cowan, N. B., Holder, G., & Kaib, N. A. 2016, ApJ, 822, L2
Famaey, B., Bruneton, J.-P., & Zhao, H. 2007, MNRAS Letters, 377, L79
Famaey, B., & McGaugh, S. S. 2012, LRR, 15, 10
Gentile, G., Famaey, B., & de Blok, W. J. G. 2011, A&A, 527, A76
Hees, A., Famaey, B., & Angus, G. W. 2016, MNRAS, 455, 449
Hees, A., Folkner, W. M., Jacobson, R. A., & Park, R. S. 2014, PhRvD, 89, 102002
Heisler, J., & Tremaine, S. 1986, Icar, 65, 13
Klioner, S. A., et al. 2021, A&A, 649, A9
Lawler, S. M., Shankman, C., & Kaib, N. 2017b, AJ, 153, 33
Lelli, F., McGaugh, S., Schombert, J. M., & Pawlowski, M. S. 2017, ApJ, 836, 152
Malhotra, R., Volk, K., & Wang, X. 2016, ApJL, 824, L22
Mardling, R. 2010, MNRAS, 407, 1048
Matthews, & Walker 1970, Mathematical Methods of Physics (New York: Benjamin)
McGaugh, S. S. 2018, arXiv:1808.09435
McGaugh, S. S., Lelli, F., & Schombert, J. M. 2016, PhRvL, 117, 201101
Milgrom, M. 1983, ApJ, 270, 365
Milgrom, M. 1986, ApJ, 306, 9
Milgrom, M. 2009, MNRAS, 399, 474
Milgrom, M. 2010, MNRAS, 403, 886
Moulton, F. R. 1984, An introduction to Celestial Mechanics (New York: Dover)
Murray, C. D., & Dermott, S. F. 2000, Solar System Dynamics (Cambridge: Cambridge Univ. Press)
Napier, K. J., Gerdes, D. W., Lin, H. W., et al. 2021, PSJ, 2, 59
Oria, P.-A., Famaey, B., Thomas, G. F., et al. 2021, ApJ, 923, 68
Penner, A. R. 2020, Ap&SS, 365, 154
Percival, I., & Richards, D. 1983, Introduction to Dynamics (Cambridge: Cambridge Univ. Press)
Petersen, J., & Lelli, F. 2020, A&A, 636, A56
Press, W. H., Flannery, B. P., Teukolsky, S. A., & Vetterling, W. T. 1998, Numerical Recipes in C (Cambridge: Cambridge Univ. Press)
Rice, M., & Laughlin, G. 2020, PSJ, 1, 81
Schwamb, M. E., Jones, R. L., Chesley, S. R., et al. 2018a, arXiv:1802.01783
Schwamb, M. E., Volk, K., Lin, H. W., et al. 2018b, arXiv:1812.01149
Shankman, C., Kavelaars, J. J., Lawler, S. M., Gladman, B. J., & Bannister, M. T. 2017, AJ, 153, 63
Sheppard, S. S., & Trujillo, C. 2016, AJ, 152, 221
Skordis, C., & Zlosnik, T. 2021, PhRvL, 127, 161302
Standish, E. M. 1993, AJ, 105, 2000
Trujillo, C. A., & Sheppard, S. S. 2014, Natur, 507, 471
Turyshev, S. G., Toth, V. T., Kinsella, G., et al. 2012, PhRvL, 108, 241101
Zhu, Y., Ma, H.-X., Dong, X.-B., et al. 2023, MNRAS, 519, 4479